

A free-form patterning method enabling endothelialization under dynamic flow

Xi Wu^a, Silvia Moimas^c, Raoul Hopf^a, Costanza Giampietro^{a,b}, Andreas Kourouklis^a, Volkmar Falk^d, Edoardo Mazza^{a,b,**}, Aldo Ferrari^{a,b,c,*}

^a ETH Zurich, Institute for Mechanical Systems, Leonhardstrasse 21, 8092, Zurich, Switzerland

^b Empa, Swiss Federal Laboratories for Materials Science and Technology, Überlandstrasse 129, 8600, Dübendorf, Switzerland

^c ETH Zurich, Laboratory of Thermodynamics in Emerging Technologies, Sonneggstrasse 3, 8092, Zurich, Switzerland

^d ETH Zurich, Department of Health Science and Technology, Tannenstrasse 3, 8092, Zurich, Switzerland

ARTICLE INFO

Keywords:

Breath figures
Endothelialization
Topography
Wall shear stress
Disturbed flow

ABSTRACT

Endothelialization strategies aim at protecting the surface of cardiovascular devices upon their interaction with blood by the generation and maintenance of a mature monolayer of endothelial cells. Rational engineering of the surface micro-topography at the luminal interface provides a powerful access point to support the survival of a living endothelium under the challenging hemodynamic conditions created by the implant deployment and function. Surface structuring protocols must however be adapted to the complex, non-planar architecture of the target device precluding the use of standard lithographic approaches. Here, a novel patterning method, harnessing the condensation and evaporation of water droplets on a curing liquid elastomer, is developed to introduce arrays of microscale wells on the surface of a biocompatible silicon layer. The resulting topographies support the *in vitro* generation of mature human endothelia and their maintenance under dynamic changes of flow direction or magnitude, greatly outperforming identical, but flat substrates. The structuring approach is additionally demonstrated on non-planar interfaces yielding comparable topographies. The intrinsically free-form patterning is therefore compatible with a complete and stable endothelialization of complex luminal interfaces in cardiovascular implants.

1. Introduction

Upon deployment in contact with organs and tissues, synthetic body implants face the inherent challenges of integration and compatibility [1]. The inflammatory response driven by the recognition of a foreign body [1,2] constitutes a threat both to the recipient, causing pain and discomfort, and to the device, frequently leading to premature revisions [3]. In the case of cardiovascular implants interacting with blood, such as vessel stents and ventricular assist devices (VADs), metallic and polymeric interfaces can trigger coagulation and thrombosis, endangering the patient's life and impairing the device's function [4]. To keep such dangers at bay, cardiovascular patients are treated with anticoagulants, in turn exposing them to the risk of hemorrhages [5].

An alternative strategy aims at the long-term integration of cardiovascular implants through the generation of a protective biological layer, able to prevent noxious signals at the luminal device interface [6].

The ideal solution consists in the generation of a fully confluent and mature monolayer of autologous endothelial cells (ECs), obtained through the process of endothelialization [7], and providing control of blood homeostasis [8,9]. Endothelialization protocols face two major challenges along their path towards clinical implementation. Firstly, cardiovascular implant deployment and function can generate regions of non-physiological, disturbed hemodynamics characterized by steep variations of flow intensity (i.e. the wall shear stress; WSS) and directionality [10,11] which prove detrimental to EC survival [12]. While in physiological conditions ECs naturally adapt to flow, by collectively orienting their cell body and polarizing their internal functions [13–15], regions of disturbed flow represent hotspots for endothelial denudation and the onset of inflammation [16]. Any successful endothelialization strategy must therefore ensure the maintenance of a confluent monolayer in regions of disturbed flow.

Tuning fluid dynamic boundary conditions by means of surface

* Corresponding author. ETH Zurich, Institute for Mechanical Systems, Leonhardstrasse 21, 8092, Zurich, Switzerland.

** Corresponding author. ETH Zurich, Institute for Mechanical Systems, Leonhardstrasse 21, 8092, Zurich, Switzerland.

E-mail addresses: mazza@imes.mavt.ethz.ch (E. Mazza), aldo.ferrari@ethz.ch (A. Ferrari).

structures is a well-studied engineering problem whereby, for example, dimpled surfaces are generated to control heat transfer [17,18]. Arrays of orderly-arranged circular microscale pits with defined diameter, depth, and spacing produce multiple vortex pairs that evolve as the flow travels downstream. This augments the local Nusselt number distribution and improves convective heat transfer on the surface [19]. The micro-scale flow-diversion induced by surface structuring may be used to locally mitigate the effect of macro-scale variation of flow intensity and directionality on ECs. Yet, this approach has not been applied in endothelialization strategies for cardiovascular implants.

A second challenge regards the upscaling of the selected topographies to cover the entire luminal surface of target cardiovascular devices. Microscale surface geometries have been successfully devised to promote endothelialization through the interaction with integrin-based adhesions (the focal adhesions [20]). Contact guidance induced by anisotropic geometries, such as gratings, enhances EC adhesion [21], spreading [22], migration [23], proliferation [24], monolayer maturation [25], and resistance to flow [24,26–28]. However, regular arrays of topographic features in the microscale [24,26] cannot be transferred on complex three-dimensional (3D) surfaces by means of standard lithographic protocols [29] and their implementation requires alternative fabrication approaches.

Elastomeric substrates, such as silicones, are applied at the luminal surface of cardiovascular implants providing the required level of deformability and supporting the process of endothelialization [6]. The silicone polymer, obtained through the process of curing, features covalent bonds between long-chain molecules [30]. Upon polymerization, the bulk material slowly evolves from a viscous liquid to an elastic solid. Towards the end of curing the elastomer still exhibits low stiffness and the nucleation of water droplets by means of condensation is sufficient to create imprints on the surface [31,32]. As curing proceeds, the droplet imprints are locked-in, even after the droplet evaporation, generating a typical topographic pattern of so called “breath figures” (BF) [33,34]. Notably, droplet nucleation occurs homogeneously at the silicone interface and is not restricted to planar surfaces. Thus, BF formation on elastomeric interfaces opens to the generation of free-form topographic patterns.

Here, we adapted and optimized a protocol for the generation of BF on biocompatible silicone substrates to form arrays of topographic features with size and spatial distribution compatible with flow-diversion at cell length scale. Diverging structures shall create continuously changing local flow conditions which dampen the noxious signals arising upon sharp hemodynamic variations. Endothelialization performance on BF-patterned surfaces was assessed challenging fully mature primary human endothelia by steep variations of WSS or flow directionality in a custom-developed bioreactor. The experimental results showed superior compliance of monolayers interacting with BF, under conditions causing denudation of control, flat substrates. In addition, the scalability and viability of the fabrication method was demonstrated for curved 3D surfaces, altogether opening to the direct patterning on free-form interfaces with superior endothelialization performance.

2. Materials and methods

2.1. Fabrication of breath figures

Any material that can spontaneously and irreversibly transition from a liquid to a solid state at a temperature close to room temperature (RT) is a candidate for the generation of breath figures (BF). Conventionally, the BF topography is generated by casting a solvent on already cured polymer, followed by droplet condensation on the dissolved substrate [35]. Here, an innovative approach of condensing droplet on curing elastomers is introduced.

The rationale supporting the selection of elastomers is based on the possibilities to cast them in liquid form on non-planar surfaces and to finely control their curing process. Specifically, the RT Vulcanizing

(RTV) silicone exhibits an ideal combination of material properties and biocompatibility [36] for the application to body implants. In addition, manufacturability at RT and relatively short curing time, facilitate faster development cycles.

The RTV silicone RTV4420 A + B (Elkem silicone, France) was used to generate BF-patterned substrates. The RTV silicone is recommended for mixing only at a 1:1 ratio [37]. The procedure generates substrates with a thermal capacity of $1300\text{--}1500\text{ J K}^{-1}\text{ kg}^{-1}$ and a conductive heat transfer coefficient of approximately $0.2\text{ W m}^{-2}\text{ K}^{-1}$ at $23\text{ }^{\circ}\text{C}$ [38,39]. Components RTV4420 A and RTV4420 B were thoroughly mixed in a 1:1 mass ratio, degassed (5 min) and spin-coated onto the target supports. Spin coating was performed on a custom-made spin-coating device, comprised of a DC motor controlled by an Arduino board (Arduino, USA). The interface between the motor and the spin-coated pieces was custom designed and 3-D printed (Prusa Research, Czech Republic). The spin-coating protocol was adjusted to achieve an approximately 60 μm thick and homogeneous coating thickness.

For the formation of BF, the environmental temperature (T) and relative humidity (RH) were controlled as follows. After initial handling of the material at RT (approximately $23\text{ }^{\circ}\text{C}$) for a desired time (indicated as t_{RTcure}) the samples were either cured at RT, or the temperature was elevated at $35\text{ }^{\circ}\text{C}$ for t_{HTcure} to accelerate the curing process. Samples were then rapidly cooled in a freezer ($-20\text{ }^{\circ}\text{C}$ for 5 min) to facilitate the subsequent droplet nucleation. Subsequently, the samples were immediately transferred to a dedicated environmental chamber at $32\text{ }^{\circ}\text{C}$ and 100% RH, sustained by a heated water bath, for a specific time (indicated as t_{humid}). Samples were kept in the environmental chamber until the silicone was fully cured. The protocol parameters t_{RTcure} , t_{HTcure} and t_{humid} were dependent on the thermal capacity and conductive heat-transfer coefficient of the substrate and were adjusted to obtain different topographies. The corresponding characterization curve of t_{RTcure} and t_{HTcure} is reported in the Supplementary Material (Figure S1). The resulting surface geometry featured a pattern of moon-crater wells (Fig. 1a and c). The protocols and parameters applied to achieve the target topography on planar and non-planar substrates are reported in Table 1.

To fabricate the substrates for flow experiments, a $126 \times 70\text{ mm}^2$ rectangle was cut from 120 μm -thick cyclic olefin copolymer (COC) foil (Ibidi, Germany). 5 g of mixed RTV was applied on the surface and evenly spread. The spin-coating speed was linearly ramped from 0 rpm to 700 rpm in the first 30 s, then maintained for additional 60 s. Following the spin-coating process, the BF-fabrication protocol in Table 1 was then applied depending on different target topography. To obtain combined surfaces featuring juxtaposed BF-pattern and flat surface areas, a hovering mask was used to limit air access on half of the surface. In this way, water nucleation was hampered on the masked surface due to restricted airflow. After the patterning process, a patch with the dimensions of $30\text{ mm} \times 15\text{ mm}$ was cut from the center of the substrate.

To prepare the patterned quarter tube, a Poly(methyl methacrylate) (PMMA) tube with inner diameter of 11 mm, wall thickness of 2 mm and length of 24 mm was evenly separated into four quarters as shown in Fig. 7a. 1 g of mixed RTV was applied on the upper side (negative curvature side) of the tube and evenly spread. The spin-coating speed was linearly ramped from 0 rpm to 700 rpm in the first 30 s, then maintained for additional 90 s. Then the BF-fabrication protocols in Table 1 were then applied depending on different target topography. To avoid uneven conductive heat transfer due to the sample curvature, it was either supported by a custom molded silicone block with full contact to the lower surface of the quarter tube or supported only at the edges.

The transfer of BF on the external surface of enameled copper wires (diameter: 0.4 mm, polysol, Elektrisola) was obtained as follows. The silicone mixture was evenly applied and spin-coated on the wires (700 rpm, 120 s without ramping). The BF-fabrication protocol in Table 1 was then applied. The wires were supported only at the edges.

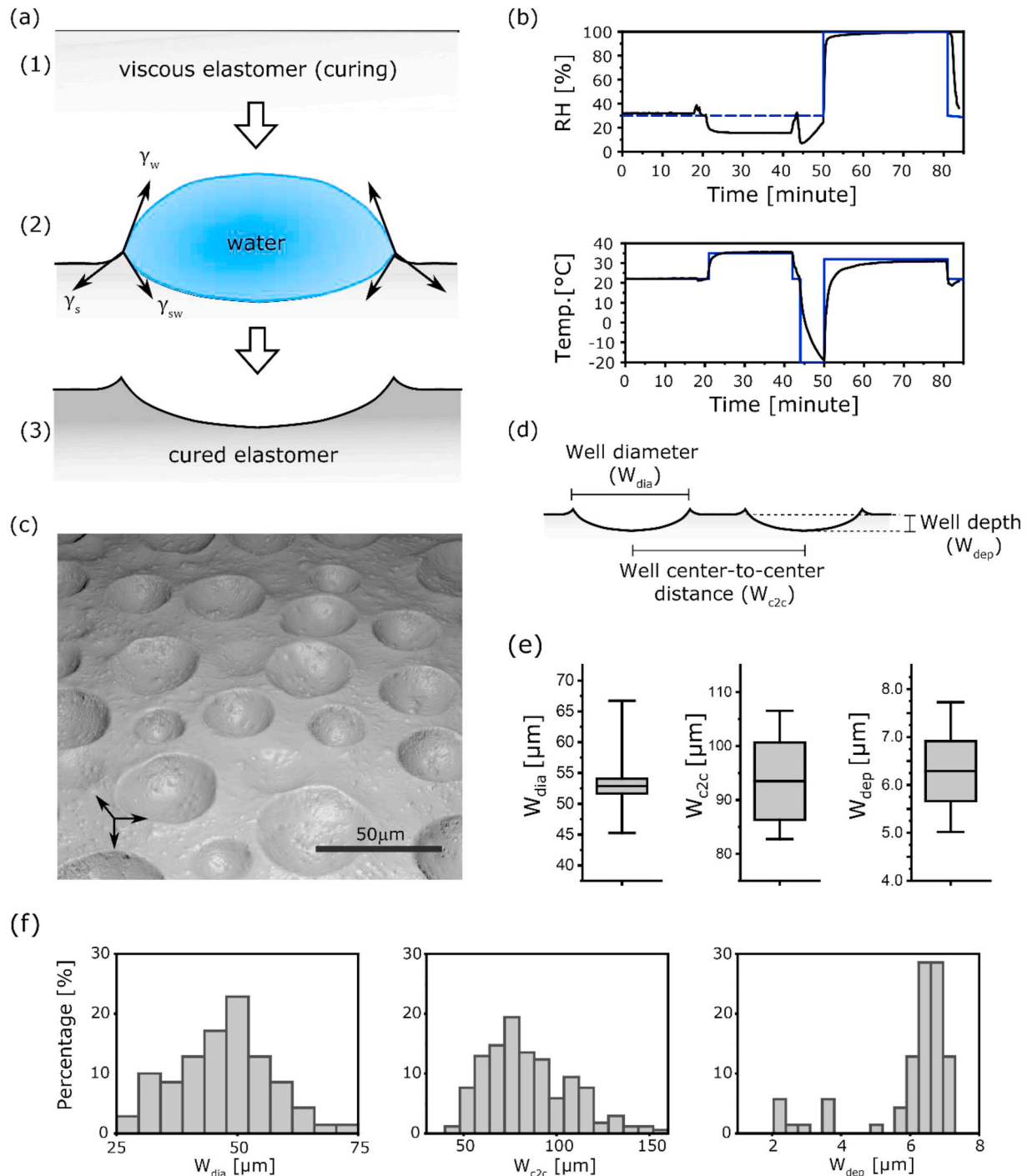


Fig. 1. Fabrication and characterization of the breath figures (BF). (a) Illustration depicting the BF formation process. (1) Uncured polymer surface, (2) nucleation of droplets upon exposure to a humid environment. Formation of droplet would deform the surface due to surface tension (γ_w water surface tension, γ_s solid surface tension and γ_{sw} interfacial surface tension between water and solid). (3) Wells formed after droplets evaporated. (b) A representative protocol used for patterning a RTV-coated cyclic olefin copolymer (COC) foil. Relative humidity (RH; top) and temperature (T; bottom) curves are reported. Legend: (—) measured (---) control target (---) no explicit control. (c) Quantitative morphology of topographic features. The image is rendered from measured height map. (d) Schematic representation of the produced topography and indications of the geometrical parameters used for the topographical characterization. (e) Box plots showing distribution of parameter means from samples used in the flow experiments. Boxes indicate mean \pm SD and whiskers indicate 5-95th percentile. (f) Distributions of parameters within one representative sample.

2.2. Substrate characterization

To characterize the BF patterns, a VK-X200 3D laser scanning confocal microscope (Keyence, Japan) [40] was used. An area of $783 \times 573 \mu\text{m}^2$ was imaged, which included on average 70 wells of 50 μm diameter in the field of view. Tilt/curvature-corrected height data were

then used to generate a height map using an in-house Matlab (Mathwork, USA) code. A threshold was manually defined using ImageJ (Fiji Edition, National Institute of Health, USA) to isolate the wells and obtain values for the well diameter (W_{dia}) and the centroid position. These data were then exported in Matlab to retrieve the depth of the well (W_{dep}) and the inter-well center-to-center distance (W_{c2c}). Specifically, W_{dep} was

Table 1

Temperature and humidity protocol. Time series of temperature and humidity parameters applied to produce flow chamber substrates, quarter tube and wire samples. * Samples were hanged in the air and only supported on the edges. ** Samples were supported by a silicone block with full contact to the lower surface of the quarter tube.

Parameter	Flow chamber substrate	Quarter-tube sample (protective)	Quarter-tube sample (shallow)	Wire
Temperature t_{RTcure} and time for spin-coating and handling	23 °C, 20 min	23 °C, 20 min	23 °C, 20 min	23 °C, 90 min
Accelerated curing temperature t_{HTcure} and time	35 °C, 21 min	35 °C, 20 min	35 °C, 20 min	none
Freezing temperature and time	−20 °C, 5 min	−20 °C, 5 min	−20 °C, 3.5 min	−20 °C, 5 min
100% Humid environment temperature and Droplet nucleation time t_{humid}	32 °C, 30min	32 °C, 30min*	32 °C, 30min**	32 °C, 20min*

measured by the height difference between the center point of the well and the flat area outside the crater. The W_{c2c} was calculated as the distance between the centers of two neighboring wells.

2.3. Gelatin–glutaraldehyde crosslinking

To enhance endothelial cell (EC) adhesion, all silicone surfaces were coated with glutaraldehyde (Sigma-Aldrich, USA)-crosslinked gelatin (#104070, Merck Millipore, Germany), as previously reported Orsenigo et al. [41]. Briefly, the samples were incubated for 1 h at 37 °C with 1.5% gelatin followed by a crosslinking with 2% glutaraldehyde solution for 15 min at RT. The glutaraldehyde was then replaced by 70% ethanol. After 1 h at RT, 5 washes with PBS (Thermo Fisher Scientific) followed by overnight incubation with PBS containing 2 mM glycine were performed. Before EC seeding, slides were washed another 5 times with PBS.

2.4. Cell culture

Human umbilical vein endothelial cells (HUVECs) were purchased from Thermo Fisher Scientific (USA) and cultured as recommended by the supplier. The cells were cultured in medium M200PRF supplemented with fetal bovine serum 2% v/v, hydrocortisone 1 mg/ml, human epidermal growth factor 10 ng/ml, basic fibroblast growth factor 3 ng/ml, and heparin 10 mg/ml (all reagents from Thermo Fisher Scientific) and maintained at 37 °C and 5% CO₂. All reported experiments were performed using cells with less than six passages *in vitro*.

Human dermal fibroblasts (HDF), isolated from adult skin, were supplied by Gibco (#C-013-5C). The cells were cultured in DMEM high glucose (4.5 g/L) medium supplemented with 10% v/v fetal bovine serum (FBS), 2 mM L-glutamine, 100 U/ml penicillin and 100 mg/ml streptomycin (all from Sigma Aldrich), maintained at 37 °C and 5% CO₂. In all reported experiments, cells with less than ten passages *in vitro* were used. HDFs were seeded on fibronectin (10 µg/ml; Sigma Aldrich, F1141) coated samples at a density of 6×10^3 cells/cm². For adhesion experiments cells were fixed 24 h after seeding whereas for differentiation experiments cells were fixed 96 h after seeding.

THP-1 cells were cultured in RPMI-1640 medium (Sigma Aldrich), supplemented with 10% v/v fetal bovine serum (FBS), 2 mM L-glutamine, 100 U/ml penicillin and 100 mg/ml streptomycin (all from Sigma Aldrich) and maintained at 37 °C with 5% CO₂. They were split every 2 or 3 days, in order to maintain their concentration around 2×10^5 cells/ml. For monocyte adhesion experiments, cells were seeded at a density of 2×10^5 cells/ml (530 cells/mm^2) in medium supplemented with 10

ng/ml of Phorbol 12-myristate 13-acetate (PMA, Sigma Aldrich), concentration required to stimulate monocyte differentiation into macrophages. Cells were fixed 72 h after seeding.

2.5. Flow experiments

ECs were seeded at high initial density (450 cell/mm^2) [25] and grown in static conditions for 72 h to generate mature monolayers, as previously reported [41,42]. Fully mature and connected endothelia, featuring similar cell density (above 560 cell/mm^2 ; [43]) and connectivity index (close to 1) represented the initial quality control and internal reference for each of the flow experiments presented. All endothelialization tests under flow were performed starting from this configuration. All samples, including the quarter-tube sample, were submerged by culturing medium in 6-well culturing plates (TPP AG, Switzerland) for cell culture.

Flow experiments with endothelial monolayers were performed in a custom-designed parallel plate flow chamber as previously described [23,28]. The flow rate was selected to reach the target WSS values, in accordance with the following equation:

$$\tau = \frac{6Q\mu}{WH^2}$$

where τ refers to the WSS, Q the volumetric flow rate, μ dynamic viscosity of water at 37 °C, W the width of the chamber and H the height of the chamber.

Specifically, cells were initially conditioned for 1 h with a flow yielding a nominal WSS of 1.4 Pa. For WSS perturbation experiments, flow was then increased to reach the WSS value of 8 Pa for 12 h, and then instantly decreased to reach the WSS of 1.4 Pa for additional 6–8 h. In flow directionality perturbation experiments, the cells were subjected to a WSS of 1.4 Pa for 12 h then the flow was inverted, to maintain the WSS of 1.4 Pa in the opposite direction, for additional 6–8 h. At the end of each experiment, the cells were fixed and immunofluorescence staining performed.

2.6. Antibodies

The following primary antibodies were used for immunofluorescence: anti-VE-cadherin (1:200, #6458) from Santa Cruz Biotechnology Inc. (USA), anti-58k Golgi protein antibody (1:100, Golgi marker, #ab27043) from Abcam (UK), anti α -SMA (1:400, #A5228) from Sigma Aldrich, anti eNOS (1:100, #610296) from BD Transduction Laboratories, anti ICAM-1 (1:100, #ab2213) from Abcam, anti YAP/YAZ (1:100, #sc-101199) from Santa Cruz Biotechnology Inc., anti Ki67 (1:400, #ab16667) from Abcam, anti β -catenin (1:100, #610154) from BD Transduction Laboratories and anti p-Y658-VEC (1:10, custom made as reported by Orsenigo et al. [41]). The secondary antibodies were rabbit anti-goat IgG (H + L) Alexa Fluor 488 (1:200; #A27012), donkey anti-mouse Alexa Fluor 555 (1:200; #A31570) conjugated, donkey anti-mouse Alexa fluor 488 (1:200, #A21202) conjugated and donkey anti-rabbit Alexa Fluor 555 (1:200, #A32794) conjugated from Thermo Fisher Scientific (USA). Phalloidin TRITC conjugated (1.25 µg/ml; #P1951) from Sigma-Aldrich was used to stain F-Actin. Cell nuclei were counterstained by DAPI (1:1000, #62248) from Thermo Fisher Scientific.

2.7. Immunofluorescence and live cell imaging

For the endpoint analysis of selected markers and cellular compartments, HUVECs were fixed for 15 min with 4% PFA in PBS. The fixed samples were subsequently permeabilized with 0.5% Triton-X100 in PBS at RT. After washing the samples three times for 5 min with PBS, they were incubated with 5% bovine serum albumin (BSA, Sigma-Aldrich, USA) in PBS for 1 h at RT. The samples were incubated with primary

antibodies overnight at 4 °C. Samples were then rinsed three times for 5 min each with 5% BSA in PBS and then incubated with the secondary antibody and DAPI for 45 min at RT. Finally, samples were washed four times (5 min each) in PBS before being stored in PBS at 4 °C until being mounted with Fluoroshield (#F6182, Sigma-Aldrich, USA) histology mounting medium and immediately imaged.

For live cell imaging of cell migration, cells were labelled with a live cell fluorogenic DNA labeling probe. The SiR-DNA probe (SC007, Spirochrome, Switzerland) was diluted at 1 μ M in complete growing medium and cells were incubated with the labeling solution for 1 h at 37 °C. The staining solution was then replaced with complete growth medium, before mounting the substrate into the flow chamber.

2.8. Image acquisition

For flow experiments, samples were imaged using an inverted Nikon-Ti spinning disk confocal microscope (Nikon, Japan) equipped with an Andor DU-888 camera (Oxford Instruments, United Kingdom) and a pE-100 LED illumination system (CoolLED Ltd, Andover, United Kingdom). A 20 \times , 0.45 NA long-distance air objective (Plan Fluor, Nikon, Japan) was used. Images were routinely acquired every 20 min in the bright-field channel for multiple positions along the sample midline. For the live cell imaging of cell migration, the setup described for the flow experiment was used. Images were routinely acquired every 20 min in the bright field channel and the far-red fluorescent channel to visualize the cell nuclei.

Images from immunostained samples were acquired with the same optical setup exploiting a 20 \times , 0.75 NA air objective (Plan Apo, Nikon, Japan) or a 40 \times , 1.3 NA oil immersion objective (Plan Fluor, Nikon, Japan) combined with FITC, TRITC and DAPI filters, for the acquisition of VE-cadherin/ β -catenin/fluorescent gelatin, Golgi/F-Actin/p-Y658-VEC, and nuclear signals, respectively.

2.9. Image analysis

To assess cell density (δ) the positions and number of nuclei within each image were measured using Imaris (Oxford Instruments, UK). Cell density was then obtained by dividing the cell number in each field of view by the area of the image.

The connectivity index (C.I.) was obtained from VE-cadherin images as previously reported [28]. The C.I. values were normalized with respect to the static control, consisting of a fully mature EC monolayer on flat surface. C.I. values close to 1 are indicative of a monolayer with a fully retained network of cell-to-cell junctions, while values close to 0 report of a diffuse VE-cadherin signal in the cytoplasm, typical of cells with disassembled or immature junctions.

Cell orientation and elongation were similarly obtained from the VE-cadherin signal. The cell outline was obtained using the “polygon selections” tool of Fiji. It was then post-processed by Matlab to measure the aspect ratio (A.R.) and orientation of individual cells by fitting an ellipsoid to the cell outline. The A.R. was calculated as the ratio between the long axis to the short axis of the fitted ellipse, while the orientation was obtained as the angle between the long axis and the flow direction (for the static samples, the horizontal axis of the image was selected as the reference axis). The obtained orientation values, in degrees, have a range of 0°–90°. A value of 0° indicates parallel alignment to the flow, whereas a value of 90° corresponds to an alignment perpendicular to the flow. A mean value of 45° depicts that there is no preferential alignment.

To evaluate cell polarity the signal from the cell nuclei and the Golgi were analyzed. A custom developed algorithm in Imaris was used followed by a post-processing procedure by a Matlab code. Initially, cellular compartments were individuated using the spot detection frame-wise in Imaris. The coordinates of the compartments were then imported to Matlab, where they were processed in order to detect their relative position. Finally, a vector from the center of each nucleus to its corresponding Golgi position was defined. The vectors' angles with the

direction of flow, was then collected and plotted in the polar histogram. For the static samples, the horizontal axis of the image was selected as the reference axis (0° polarization).

To evaluate VE-Cadherin phosphorylation level, signal from β -catenin and p-Y658-VEC were used. Images were post-processed by the Image J plugin Extended Depth of Field [44] into a 2D image and corrected for background illumination. Pearson's coefficient was determined using the colocalization plug-in of Imaris. During the colocalization analysis, calculated threshold values were imposed for both the β -catenin and p-Y658-VEC channels.

To evaluate YAP/TAZ nuclear localization, signal from YAP/TAZ and nuclei were used. The same evaluation scheme as reported in Ref. [45] was used. The ratio of average nuclear and cytoplasmic YAP/TAZ signal intensity was calculated.

To evaluate HDF differentiation, the signal from α -SMA and cell nuclei were used. Cell area segmentation was done using the ‘Cell’ plugin in Imaris. Mean α -SMA signal intensity inside the individual cells was calculated.

To evaluate eNOS expression, the signal from eNOS channel was used. Cell area was manually defined using in-house Matlab code. Mean eNOS signal intensity inside the individual cells was calculated.

2.10. Cell migration assay

To quantify cell migration the nuclear fluorescence was used. Tracking nuclei in time-lapse images was performed using the ‘spot detection’ tool of Imaris. Each track was analyzed using Matlab to extract the counterflow, streamwise, and stationary components. Briefly, two subsequent frames were analyzed, and the cell displacement was calculated. Any displacement of less than 2.7 μ m was defined as stationary. Contributions of stationary, streamwise and counterflow migration steps were calculated by dividing the individual step counts by the number of total steps.

2.11. Cell adhesion assay

ECs were seeded at low density of 130 cells/mm² on gelatin cross-linked coated substrates. After 12 h of culture cells were fixed and permeabilized as stated in ‘Immunofluorescence and live cell imaging’ subsection. Cell nuclei were stained with DAPI.

2.12. Cell proliferation assay

ECs were seeded at low density of 130 cells/mm² on gelatin cross-linked coated substrates. After 24 h of culture, cells were fixed and permeabilized as stated in ‘Immunofluorescence and live cell imaging’ subsection. Cells were stained with anti-Ki67 antibody and cell nuclei were stained with DAPI.

2.13. Inflammatory response

ECs were seeded at low density of 130 cells/mm² on gelatin cross-linked coated substrates. After 24 h of culture, cells were treated with TNF- α (#300-01A, PeproTech, USA) 10 ng/ml for 24 h and then fixed and permeabilized as stated in ‘Immunofluorescence and live cell imaging’ subsection. Cells were stained with anti-ICAM-1 antibody and cell nuclei were stained with DAPI.

2.14. Cell death assay

ECs were seeded at low density of 130 cells/mm² on gelatin cross-linked coated substrates. After 12 h of culture, cells were treated with the cytotoxic agent H₂O₂ (#822287, Sigma-Aldrich, USA) 1 mM for 3 h. After removal of the toxic agent, cells were incubated with Ethidium homodimer-1 (Eth-D1, Molecular Probes E1169) 4 μ M, for 15 min at RT, cells were then fixed with 4% PFA in PBS for 15 min. Cell nuclei were

stained with DAPI. Samples were imaged at 20x magnification.

2.15. tPA secretion

ECs were seeded at high density of 450 cell/mm² on gelatin cross-linked coated substrates. Medium was changed the day after seeding to remove dead cells, then cells were kept in culture for additional 2 days to allow the maturation of the endothelial monolayer. The medium was collected, centrifuged at 2000 g for 10 min to remove cellular debris, and stored in aliquots at -20 °C. Assessment of tPA concentration in the supernatant was performed by means of human TPA ELISA kit (Abcam ab190812), following manufacturer's recommendations.

2.16. VE-cadherin phosphorylation inhibition assay

ECs were seeded at high initial density (450 cell/mm²) [25] and grown in static conditions for 72 h to generate mature monolayers, as previously reported [41,42]. The Src inhibitor PP1 (10 μM, Enzo Life Sciences, Orsenigo et al. [41]) was added 18 h before exposure to flow. The PP1-containing medium was removed immediately before the flow experiments and exchanged with fresh medium without inhibitor. The endothelial monolayers were exposed to flow generating a WSS of 1.4 Pa for 12 h and then immediately fixed for the evaluation of cell polarization (Golgi and nuclear staining) or VEC phosphorylation (β-catenin and p-Y658-VEC staining).

2.17. Gelatin stability assay

The coating procedure adopted for our endothelialization experiments represents an established standard for the cultivation of ECs [41]. It was successfully applied to support endothelialization on various materials, including substrates featuring topographic patterns of various size and geometry [21,23,24,28,46] on plastic polymers and elastomers. The protocol includes a step of crosslinking (using glutaraldehyde) which ensures stable bonding of gelatin to the substrate with no peeling off or release even at high WSS values (up to 10 Pa [28]). The same procedure was applied to deformable elements of a blood pump, which were tested for endothelialization performance *in vivo*, therefore showing compatibility and stability also in contact with blood [47]. The coating homogeneity on BF substrates and its retention under flow was confirmed by dedicated experiments (Supplementary Material Figure S2), in which fluorescently labelled gelatin (gelatin from pig skin, Fluorescein Conjugate, #G13187, Thermo Fisher Scientific, USA) was mixed at 1:10 with the non-labelled counterpart and crosslinked on silicone surface following the coating procedure reported in Orsenigo et al. [41]. Confocal fluorescence Z-stacks (step height ΔZ = 0.2 μm) were collected before and after exposure to flow generating a WSS of 1.4 Pa.

2.18. Statistical analysis

Statistical comparison of δ, C.I., A.R., orientation and cell migration on BF-patterned substrates and corresponding flat counterparts were performed using a nonparametric Mann-Whitney test. All quantitative measurements reported as box plots are expressed as average values ± standard deviation (SD; box), with the whiskers extending from the 5th to the 95th percentiles. All quantitative measurements reported as bar plots are expressed as average values ± standard error of the mean (s.e. m). The total number of cells analyzed is indicated as n and the number of independent experiments as N, and they are reported in the corresponding figure legends. All statistical analysis was performed using Origin (OriginLab, USA) and p less than 0.05 was considered significant (*p < 0.05, **p < 0.01, ***p < 0.001).

3. Results

3.1. Generation of BF: condensation of droplets as patterning template

Elastomers, such as rubbers and silicones, are versatile materials that can be used for implantable medical devices (as reviewed in Ref. [34]). Elastomer surfaces might provide a favorable interface with the biological components of living systems. In particular, the room temperature vulcanizing (RTV) 4420 silicone displays low cytotoxicity [36] and represents a viable substrate for endothelialization [6]. However, conventional patterning protocols, like those based on standard lithography, cannot be applied to introduce topographic features on complex, 3D RTV surfaces. To support endothelialization, we aimed at generating a regular array of circular wells by means of BF formation upon material curing (Fig. 1a). Based on our previous work on planar surfaces [24], target values for the resulting topographic features were set to an average well diameter (W_{dia}) of 40 μm and well depth (W_{dep}) of 6 μm. These feature sizes allow for the formation of fully connected endothelia [24].

In a series of preliminary tests, environmental temperature (T) and relative humidity (RH) were tuned to adjust the size of resulting BF wells. The elastomer viscosity also plays a key role and it varies as function of time, given the same curing condition [48]. The optimization of these parameters yielded the selection of specific time functions for T and RH (Fig. 1b). The substrates were initially prepared at room T and RH. After a first phase of curing at 23 °C and 35 °C for a total of 41 min, they were cooled down to -20 °C for 5 min. This passage supported droplet nucleation in the ensuing phase, obtained by increasing RH to 100% and T to 32 °C for 30 min. All conditions applied in the fabrication process are reported in Table 1.

The resulting surface geometry featured a pattern resembling moon-crater wells (Fig. 1c). While the W_{dia} and the center-to-center distance (W_{c2c}, as illustrated in Fig. 1d) displayed a relatively broad distribution with average values of 52.9 ± 5.1 μm and 93.5 ± 7.2 μm, respectively, the W_{dep} closely matched the target value (6.3 ± 0.6 μm) with a narrow distribution (Fig. 1e and f). The values of these topographic descriptors in individual samples used for endothelialization experiments are reported in Table 2.

An extensive parametric study was additionally performed to

Table 2

BF topography characterization. Analysis of the topography parameters for each individual sample used in the flow experiments. *Samples produced with shallower topography.

Sample number	Well diameter (m) W _{dia} (Mean ± SD)	Well center-to-center distance (m) W _{c2c} (Mean ± SD)	Well depth (m) W _{dep} (Mean ± SD)
1	51.92 ± 12.47	91.29 ± 24.99	6.63 ± 1.89
2	48.69 ± 13.31	90.41 ± 24.14	6.96 ± 2.43
3	50.20 ± 13.71	85.13 ± 23.07	6.90 ± 2.54
4	46.86 ± 9.85	84.60 ± 22.72	5.96 ± 1.35
5	53.81 ± 14.26	99.29 ± 25.12	6.45 ± 2.04
6	49.06 ± 11.00	89.17 ± 23.37	7.73 ± 1.67
7	66.73 ± 12.15	106.52 ± 21.68	6.20 ± 1.13
8	55.06 ± 10.54	92.76 ± 19.69	5.82 ± 1.52
9	54.13 ± 9.90	91.96 ± 21.49	5.60 ± 1.27
10	54.58 ± 9.16	90.31 ± 24.03	6.54 ± 1.50
11	48.09 ± 9.48	82.75 ± 21.35	6.45 ± 1.40
12	59.64 ± 11.47	97.01 ± 22.62	6.64 ± 2.08
13	53.15 ± 8.03	98.80 ± 33.34	5.96 ± 1.14
14	55.23 ± 11.20	102.54 ± 33.85	6.27 ± 1.5
15	57.19 ± 9.87	105.55 ± 38.97	5.53 ± 1.00
16	49.46 ± 9.24	92.40 ± 29.69	6.65 ± 1.44
17	52.63 ± 9.28	97.44 ± 36.32	5.91 ± 1.03
18	45.27 ± 11.60	84.88 ± 33.82	5.02 ± 1.68
19*	62.40 ± 14.15	109.19 ± 35.29	4.68 ± 1.18
20*	73.64 ± 12.01	131.25 ± 41.22	4.33 ± 0.94
21*	65.88 ± 14.67	119.44 ± 38.80	4.40 ± 0.99

evaluate the variation of the topographic descriptors as function of the curing T and RH (Supplementary Material Figure S1). This data demonstrate that the BF fabrication process is flexible and allows the generation of BF-patterned with desired variations of topographic feature size and distribution.

3.2. Endothelialization of BF substrates

To demonstrate the viability of BF-patterned substrates, primary human umbilical vein endothelial cells (HUVECs) were seeded at high density. After 3 days of static culture, the formation of confluent and mature monolayers was evaluated by means of immunofluorescence, in comparison with otherwise identical, but flat, control substrates (Fig. 2). Specifically, the cell density (δ), the establishment of adherens junctions (AJs, i.e. the monolayer connectivity, measured by the connectivity index C.I. [28]), the cell shape (measured by the cell aspect ratio A.R. and the collective cell orientation), and the planar cell polarization (i.e. the relative position of the Golgi apparatus and the cell nucleus) were assessed.

Small differences were observed between monolayers formed on the BF-patterned substrates and the corresponding control (Fig. 2). Under static conditions, ECs cultured on BF reached higher density ($\delta = 783 \pm 17$ cells/mm²) than those on flat surface ($\delta = 623 \pm 17$ cells/mm², Fig. 2a). The cell-to-cell junction distribution was not affected by the topography. Indeed, both systems formed well-connected networks of cell-to-cell junctions (C.I. = 1.1 ± 0.1 and 1.0 ± 0.1 on BF or flat substrates, respectively, Fig. 2b and c) indicating full maturity of the endothelia (Fig. 2f). On BF-patterns, 1–2 ECs occupied each well, as can be appreciated in Fig. 2c. As expected, cells on control substrates were only slightly elongated (A.R. 1.92 ± 0.69 ; Fig. 2d) and no preferential collective orientation ($46 \pm 25^\circ$; Fig. 2e and f) or polarizations were detected (Fig. 2g and h). The interaction with BF did not significantly alter these values, and ECs were rather round (A.R. 1.74 ± 0.46 ; Fig. 2d) with random orientation ($42 \pm 25^\circ$) and polarization (Fig. 2e and f, and Fig. 2g and h, respectively).

Molecular markers were used to assess the cell viability when treated with H₂O₂ (Fig. 2i), cell proliferation capacity (Fig. 2j and k), the homeostatic function [49] based on the production of tissue-type plasminogen activator (tPA; Figure 2l) and the levels of endothelial nitric oxide synthase (eNOS) expression (Figure 2o). In addition, EC adhesion (Figure 2p and q), activation state of the YAP/TAZ mechanotransduction pathway (Figure 2m and n [50,51]) and the response to inflammatory stimuli (Figure 2r and s) were included in the evaluation. No significant variations in these functional descriptors were detected between ECs contacting flat or BF-patterned substrates.

To extend the characterization of BF-patterned substrates, the adhesion of Human Dermal Fibroblasts (HDF) and THP-1 monocytes were evaluated (Supplementary Material Figure S3a, S3b, S3e and S3f, respectively). No significant changes were detected in comparison with identical flat substrates. In addition, the differentiation of HDFs into myofibroblasts was assessed revealing the expression of α -smooth muscle actin (α -SMA, Supplementary Material Figure S3c and S3d). Again, no specific myofibroblast induction was detected on BF-patterned substrates.

Endothelial monolayers naturally sense and adapt to fully developed, homogenous flow [9,15,16,52,53]. This process involves coordinated cell elongation, orientation of the cell body, and polarization [28]. To evaluate the effect of BF topography on this adaptive response, mature endothelia were exposed to laminar flow generating physiological values of WSS (1.4 Pa) for 16 h.

The experimental set-up comprised a custom developed flow-chamber which can generate on demand flow conditions yielding physiological (0.1–6 Pa) and supraphysiological (6–12 Pa) WSS values as well as sharp variations of flow intensity and directionality [23]. Using this system, endothelial monolayers can be maintained and monitored under flow for up to 24 h. Longer conditioning suffers of the

intrinsic limitations of *in vitro* endothelial cultures, including the exhaustion of metabolic supply and cell over confluence, which generate experimental artifacts. However, it is demonstrated that the adaptation of endothelial monolayers to flow is typically accomplished within 12 h of conditioning, reaching a stable configuration of collective cell alignment, elongation, and polarization, which is then maintained under unaltered hemodynamic conditions [14,54,55].

The results are reported in Supplementary Material Figure S5. No significant differences in cell density and C.I. were found. As expected, ECs interacting with the flat control elongated (from A.R. = 1.73 ± 0.60 to A.R. = 2.31 ± 0.98) and oriented parallel to flow (from $43^\circ \pm 26^\circ$ – $31^\circ \pm 23^\circ$; [23,28]). On BF-patterned substrates, ECs maintained an almost unaltered morphology (from A.R. = 1.53 ± 0.36 to A.R. = 1.74 ± 0.60) with similar orientation (from $44^\circ \pm 26^\circ$ – $29^\circ \pm 21^\circ$). On both substrates the monolayer integrity was fully preserved upon interaction with flow (C.I. = 1.0 ± 0.4 and 1.1 ± 0.3 on flat or BF; respectively). On flat substrates ECs collectively polarized in the counterflow direction. The coordinated polarization was significantly reduced on the BF-patterned substrates. These results are suggestive of a disturbed or inhomogeneous directional signal conveyed by the local hemodynamic conditions to endothelial contacting BF-patterns.

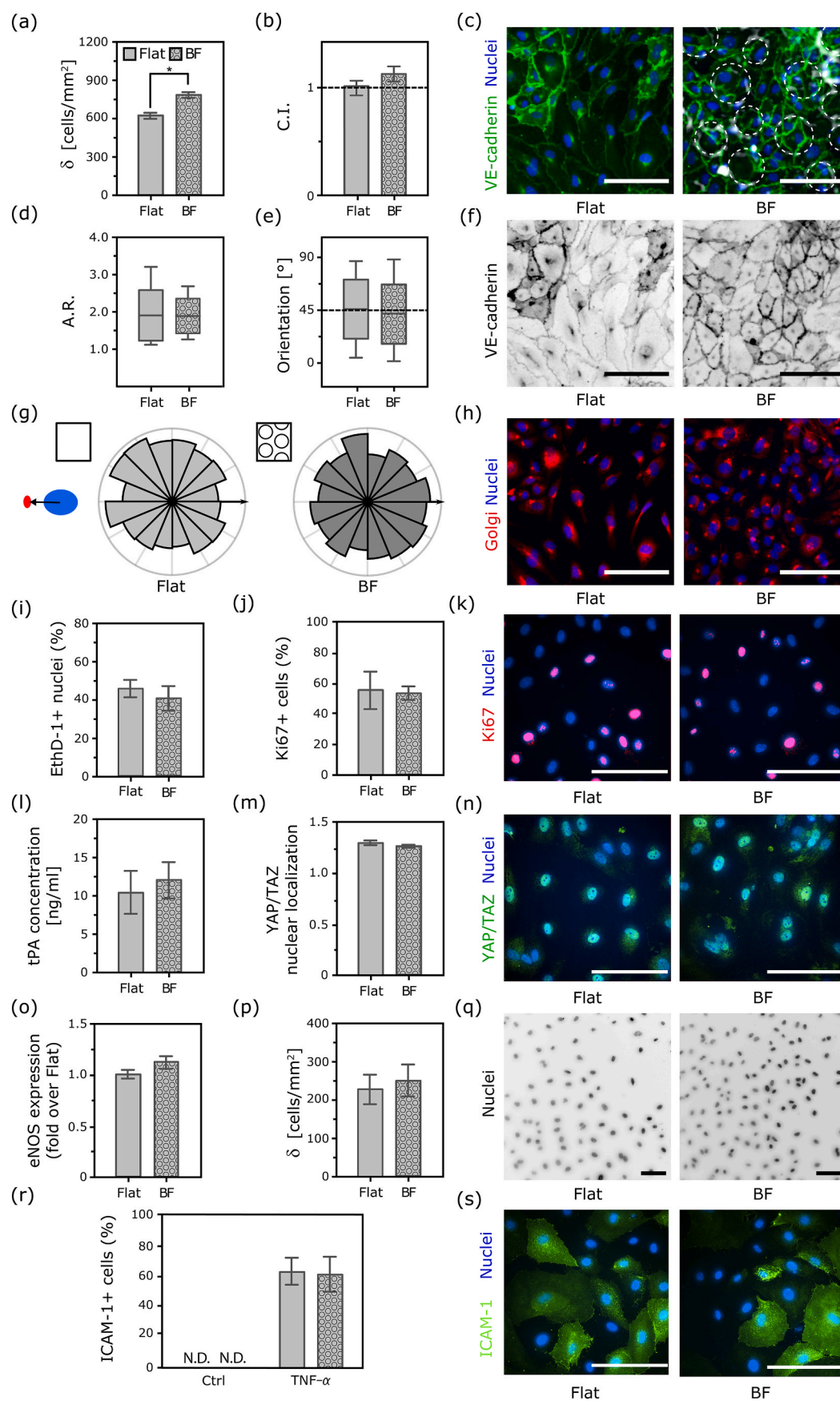
EC migration is influenced by the local topography and its interaction with flow [21]. Therefore, the collective dynamics of ECs contacting BF-patterned substrates, or their flat counterparts was monitored, and the resulting cell migrations tracks are reported in Fig. 3a. Exposure to flow induced ECs on flat substrates to migrate along the flow direction. Instead, the corresponding tracks recorded on BF patterns exhibited a more isotropic distribution. The mean length of EC migration parallel to the flow direction was here less than half (11 μ m) as compared to the control (26 μ m; Fig. 3b). To obtain further insights, individual migration tracks were classified into streamwise, stationary and counterflow components (Fig. 3c; [21]). On flat substrates, HUVECs migrated mainly along the direction of flow ($58 \pm 2\%$; Fig. 3f), while the streamwise component of migration was less represented on topography ($41 \pm 1\%$, Fig. 3f). On the other hand, ECs on BF substrates were more stationary (BF $35 \pm 1\%$, Fig. 3e) or moving against the flow ($23 \pm 1\%$, Fig. 3d) than the flat control ($25 \pm 1\%$ and $17 \pm 1\%$, for stationary and counterflow migration; respectively. Fig. 3e and d).

In summary, these data demonstrate that BF patterns do not induce measurable morphologic or functional variations upon their interaction with ECs under static conditions. Moreover, they indicate a mitigation of the local hydrodynamic signals inducing collective cell adaptation to flow.

3.3. Endothelialization performance under disturbed flow: flow directionality

When exposed to physiological WSS (below 6 Pa) ECs gradually elongate and align along the direction of flow. At supraphysiological values (above 6 Pa), an orthogonal orientation emerges and cells align perpendicular to flow [28,56]. Cell polarity follows instead the flow directionality. ECs exposed to a steady laminar flow polarize in the counterflow direction by moving the Golgi upstream of the nucleus [52]. Owing the complex cellular responses necessary to adapt to the local hemodynamic conditions, steep variations in either the flow magnitude or directionality, represent a challenge for the maintenance of tissue integrity [57,58].

To evaluate whether the reduced adaptation to flow of ECs on BF-patterned substrates (Fig. 2) enhances their resistance, the monolayers were exposed to detrimental, rapid hemodynamic variations using a custom-developed experimental setup [23,28]. In these experiments, the WSS value of 1.4 Pa, typically measured in human coronary arteries [23, 41,59], was selected as representative of physiological hemodynamic conditions. Arterial stenosis or the function of blood pumping devices can generate supraphysiological flow with higher WSS values, which were experimentally reproduced by selecting a WSS of 8 Pa.



(caption on next page)

Fig. 2. Endothelialization of BF substrates in static conditions and characterization of EC features. Results of a representative experiment are shown. Experiment repetitions $N = 3$ if not otherwise specified. (a) Quantification of cell density (δ). Fields of view quantified for each bar $n = 10$. Data are expressed as mean \pm s.e.m. (b) Quantification of the connectivity index (C.I.). Results are normalized with respect to the average value of mature monolayers on flat surfaces in static conditions. C.I. of a fully connected EC monolayer (1) is indicated by a dashed line. Number of cells quantified for each bar $n = 75$. (c) Immunostaining of EC monolayers seeded on flat (Flat, left) or BF substrates (BF, right). VE-cadherin (green) and cell nuclei (DAPI, blue). The corresponding bright field image (white) was overlaid on the BF image. The well profiles are indicated by white dashed circles. Scale bar: 100 μ m. (d) Quantification of cell aspect ratio (A.R.). Boxes indicate mean \pm SD and whiskers indicate 5-95th percentile. Number of cells quantified in each box $n = 108$. (e) Quantification of cell orientation. Number of cells quantified in each box $n = 108$. Mean orientation of randomly oriented cells (45°) is indicated by a dashed line. (f) Immunostaining of EC monolayer on flat (Flat, left) or BF substrate (BF, right). VE-cadherin (grayscale inverted). Scale bar: 100 μ m. (g) Analysis of cell polarization. Polar histograms reporting of cell polarity assessment (vector pointing from nucleus to Golgi apparatus, as depicted in the drawing) on flat (left) or BF substrate (right) in static conditions. (h) Immunostaining of endothelial cell monolayers seeded on flat (Flat, left) or BF substrate (BF, right) in static conditions, Golgi apparatus (red) and cell nuclei (DAPI, blue). Scale bar: 100 μ m. (i) Quantification of endothelial cell death in response to H_2O_2 treatment. Fields of view quantified in each bar $n = 10$. Data are expressed as mean \pm s.e.m. Dead cells are stained by the EthD-1 dye. (j) Quantification of endothelial cell proliferation. Fields of view quantified in each bar $n = 10$. Data are expressed as mean \pm SD of 3 experiments. Proliferating cells are stained for the cell cycle marker Ki67. (k) Immunostaining of EC seeded at subconfluent density on flat (Flat, left) or BF substrate (BF, right). Ki67 (red) and cell nuclei (DAPI, blue). Scale bar: 50 μ m. (l) Quantification of tPA released in the supernatant by EC monolayers formed on flat (Flat) or BF substrates. Data are expressed as mean \pm s.e.m. The concentration of tPA was quantified by means of ELISA assay. (m) Quantification of YAP/TAZ nuclear localization. Fields of view quantified in each bar $n = 10$. Data are expressed as mean \pm s.e.m. (n) Immunostaining of EC monolayers seeded on flat (Flat, left) or BF substrate (BF, right). YAP/TAZ (green) and cell nuclei (DAPI, blue). Scale bar: 50 μ m. (o) Quantification of eNOS expression. Fields of view quantified in each bar $n = 10$. $N = 2$. Data are expressed as mean \pm s.e.m. (p) Quantification of EC adhesion. Fields of view quantified in each bar $n = 10$. Data are expressed as mean \pm s.e.m. (q) Immunostaining of EC seeded at subconfluent density on flat (Flat, left) or BF substrate (BF, right). Cell nuclei (DAPI, grayscale inverted). Scale bar: 50 μ m. (r) Quantification of ICAM-1 expression in response to TNF- α treatment. Fields of view quantified in each bar $n = 10$. $N = 2$. Data are expressed as mean \pm SD of 2 experiments. In absence of TNF- α treatment ECs do not express the adhesion molecule ICAM-1 (N.D. not detectable). (s) Immunostaining of EC seeded at subconfluent density on flat (Flat, left) or BF substrate (BF, right). Representative images of EC treated with TNF- α are reported. ICAM-1 (green) and cell nuclei (DAPI, blue). Scale bar: 50 μ m * $p < 0.05$. (For interpretation of the references to colour in this figure legend, the reader is referred to the Web version of this article.)

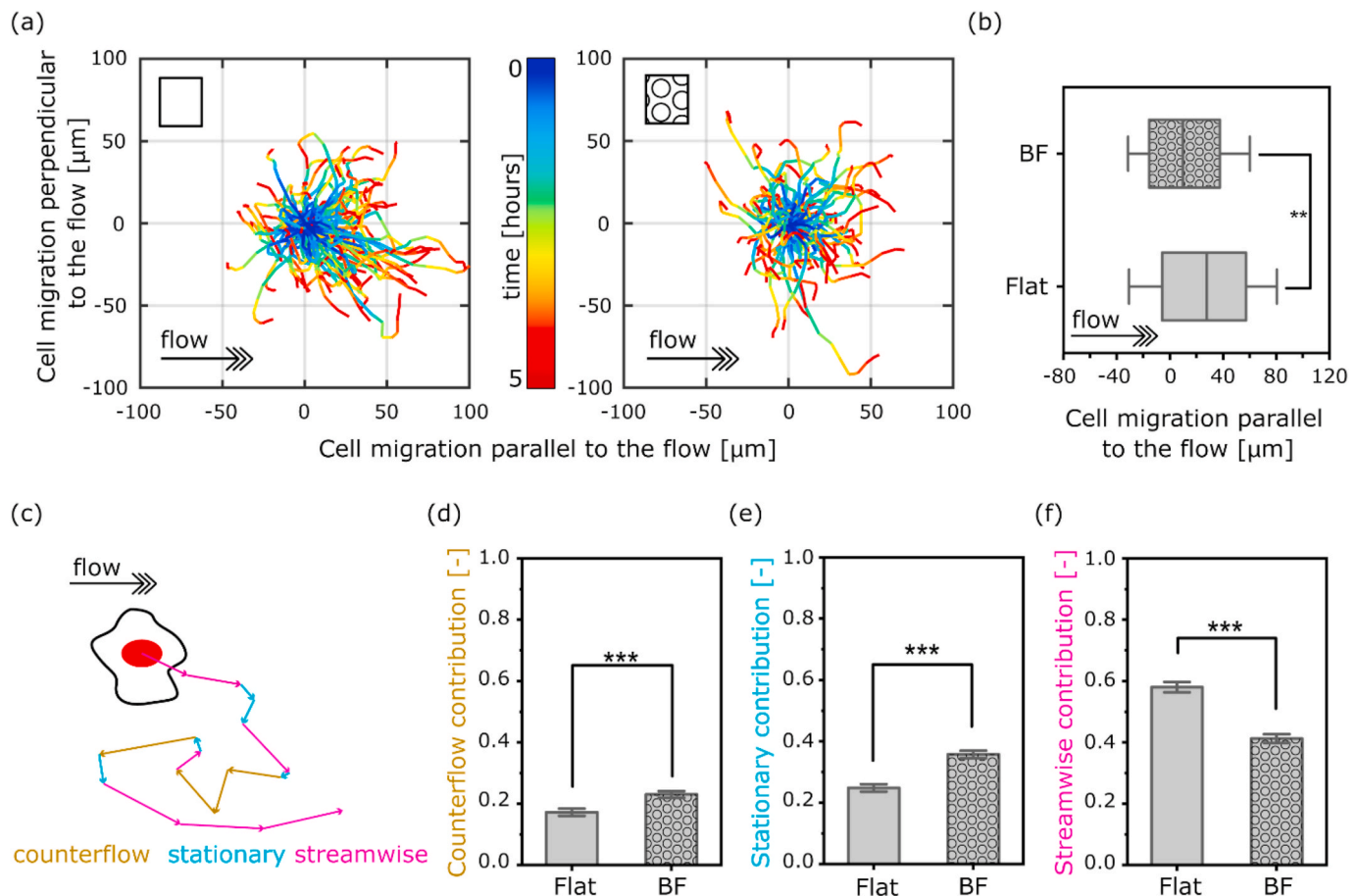


Fig. 3. EC migration under flow (WSS 1.4 Pa). (a) Tracks extracted from time-lapses (for a total of 5 h) of HUVECs on flat (left) or BF substrates (right). The arrow indicates the flow direction. (b) Total migration parallel to the flow generating a WSS of 1.4Pa. Boxes indicate mean \pm SD and whiskers indicate 5-95th percentiles. (c) Cartoon depicting counterflow, stationary and streamwise components of individual trajectories. (d-f) Quantifications of trajectory components: (d) counterflow contribution, (e) stationary contribution and (f) streamwise contribution. Data are reported as mean \pm s.e.m. ** $p < 0.01$, *** $p < 0.001$.

A first set of endothelialization tests was designed to investigate the monolayer retention upon inversion of the flow direction. The experimental setup is shown in [Supplementary Material Figure S4a and S4b](#). A

continuous endothelial monolayer was generated on a RTV substrate featuring a BF-patterned surface longitudinally juxtaposed to a corresponding flat region. Mature endothelia were initially exposed to a

steady-state laminar flow generating a WSS of 1.4 Pa. After accomplishment of full adaptation to this condition (12 h; [54]) the flow directionality was switched and the monolayer was exposed to an inverted flow of the same magnitude for an additional period (8 h).

The response to the switch was dramatically different for ECs in the two regions of the substrate (Supplementary Material Video S1 and S2).

The monolayer integrity was rapidly compromised on the flat surface, as described by a drop of cellular density (from $\delta = 522 \pm 29$ cells/mm² to $\delta = 455 \pm 57$ cells/mm²) and a significant reduction in connectivity (from C.I. = 1.0 ± 0.1 to C.I. = 0.7 ± 0.1 ; Fig. 4a and b, respectively). In addition, the immunofluorescence analysis revealed the presence of multiple gaps between neighboring cells, indicating an ongoing

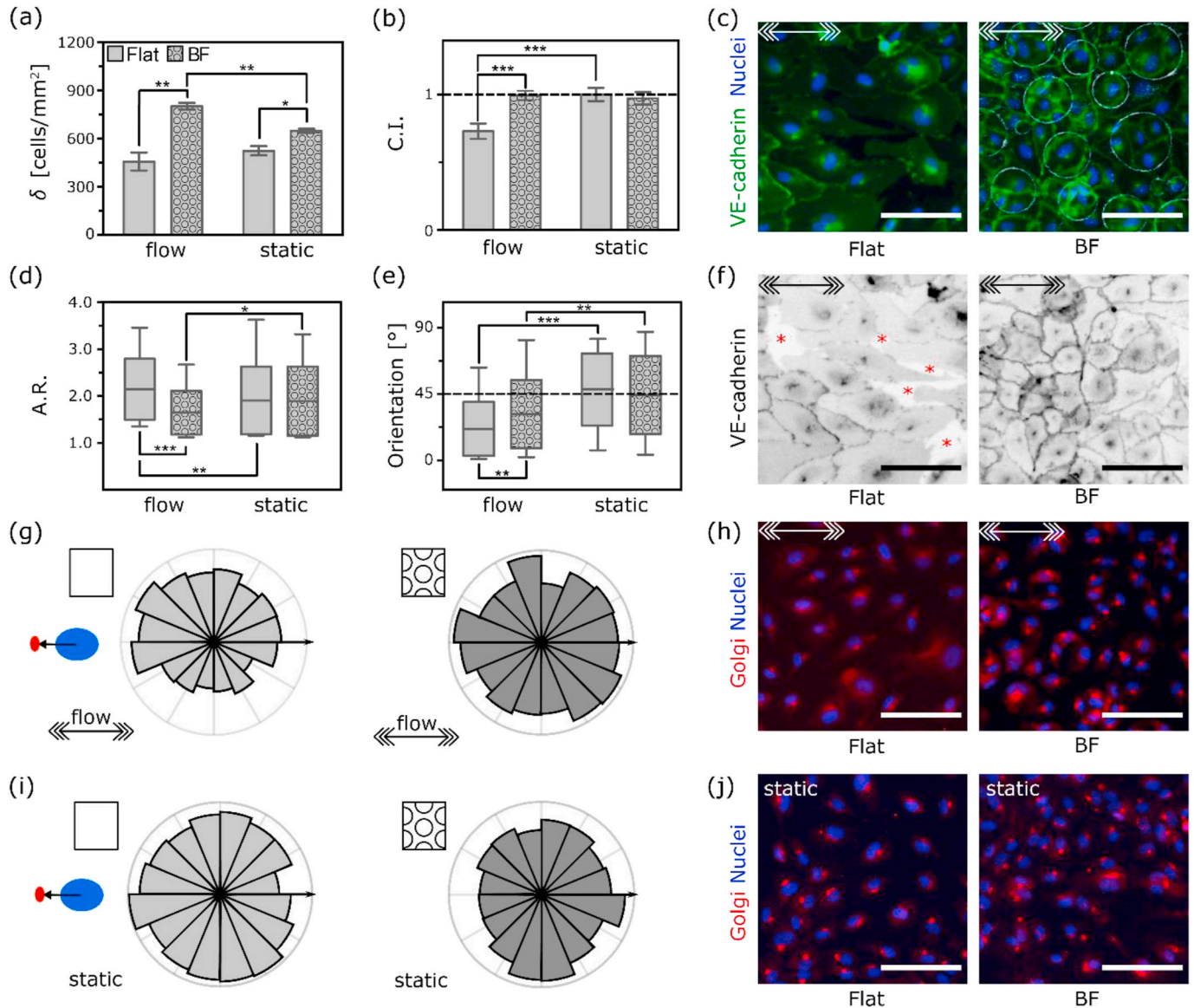


Fig. 4. Effect of flow directionality on EC monolayer. Mature monolayers were exposed to an initial flow of 1.4Pa WSS for 12 h. The flow direction was then inverted to maintain the WSS of 1.4 Pa in the opposite direction, for additional 6–8 h. Results of a representative experiment are shown. Experiment repetitions $N = 3$, data corresponding to the independent repetitions can be found in [Supplementary Material Figure S6](#). (a) Quantification of cell density (δ). Fields of view quantified in each bar $n = 10$. Data are expressed as mean \pm s.e.m. (b) Quantification of the connectivity index (C.I.). Number of cells quantified in each bar $n = 60$. C.I. of a fully connected EC monolayer (1) is indicated by a dashed line. (c) Immunostaining of EC monolayers seeded on flat (Flat, left) or BF substrates (BF, right). VE-cadherin (green) and cell nuclei (DAPI, blue). The corresponding bright field image (white) is overlaid on the BF image. The arrow indicates the flow direction. Scale bar: 100 μ m. (d) Quantification of cell aspect ratio (A.R.). Boxes indicate mean \pm SD and whiskers indicate 5–95th percentile. Number of cells quantified in each box $n = 108$. (e) Quantification of cell orientation. Number of cells quantified in each box $n = 108$. Mean orientation of randomly oriented cells (45°) is indicated by a dashed line. (f) Immunostaining of EC monolayer on flat (Flat, left) or BF substrates (BF, right). VE-cadherin (grayscale inverted). The presence of gaps in the monolayer is highlighted by red asterisks. The arrow indicates the flow direction. Scale bar: 100 μ m. (g) Analysis of cell polarization under flow. Polar histograms reporting cell polarity assessment (vector pointing from nucleus to Golgi apparatus, as depicted in the drawing) on flat (left) or BF substrates (right). The arrow indicates the flow direction. Approximately $n = 1500$ cells were analyzed in each polar diagram. (h) Immunostaining of endothelial monolayer on flat (Flat, left) or BF substrates (BF, right) subjected to flow. Golgi apparatus (red) and cell nuclei (DAPI, blue). Scale bar: 100 μ m. (i) Analysis of cell polarization in static conditions. Polar histograms reporting cell polarity assessment (vector pointing from nucleus to Golgi apparatus, as depicted in the drawing) on flat (Flat; left) or BF substrates (BF; right) in static conditions. (j) Immunostaining of EC monolayers seeded on flat (Flat, left) or BF substrate (BF, right) in static conditions, Golgi apparatus (red) and cell nuclei (DAPI, blue). Scale bar: 100 μ m * $p < 0.05$, ** $p < 0.01$, *** $p < 0.001$. (For interpretation of the references to colour in this figure legend, the reader is referred to the Web version of this article.)

substrate denudation (Fig. 4c). On the contrary, the cellular density and the cell-to-cell junctions were fully preserved on BF substrate, presenting slightly increased values ($\delta = 798 \pm 21$ cells/mm² and C.I. = 1.0 ± 0.1). Individual ECs on the flat region were more elongated (A.R. = 2.14 ± 0.64) and better oriented along the flow direction ($21^\circ \pm 18^\circ$, Fig. 4d, e and 4f) as compared to those on BF (A.R. = 1.64 ± 0.46 and orientation

$31^\circ \pm 23^\circ$, Fig. 4d and e, respectively). Finally, cell polarization was randomly distributed, with no commitment to a specific direction (Fig. 4g and h. Corresponding static control data shown in Fig. 4i and j).

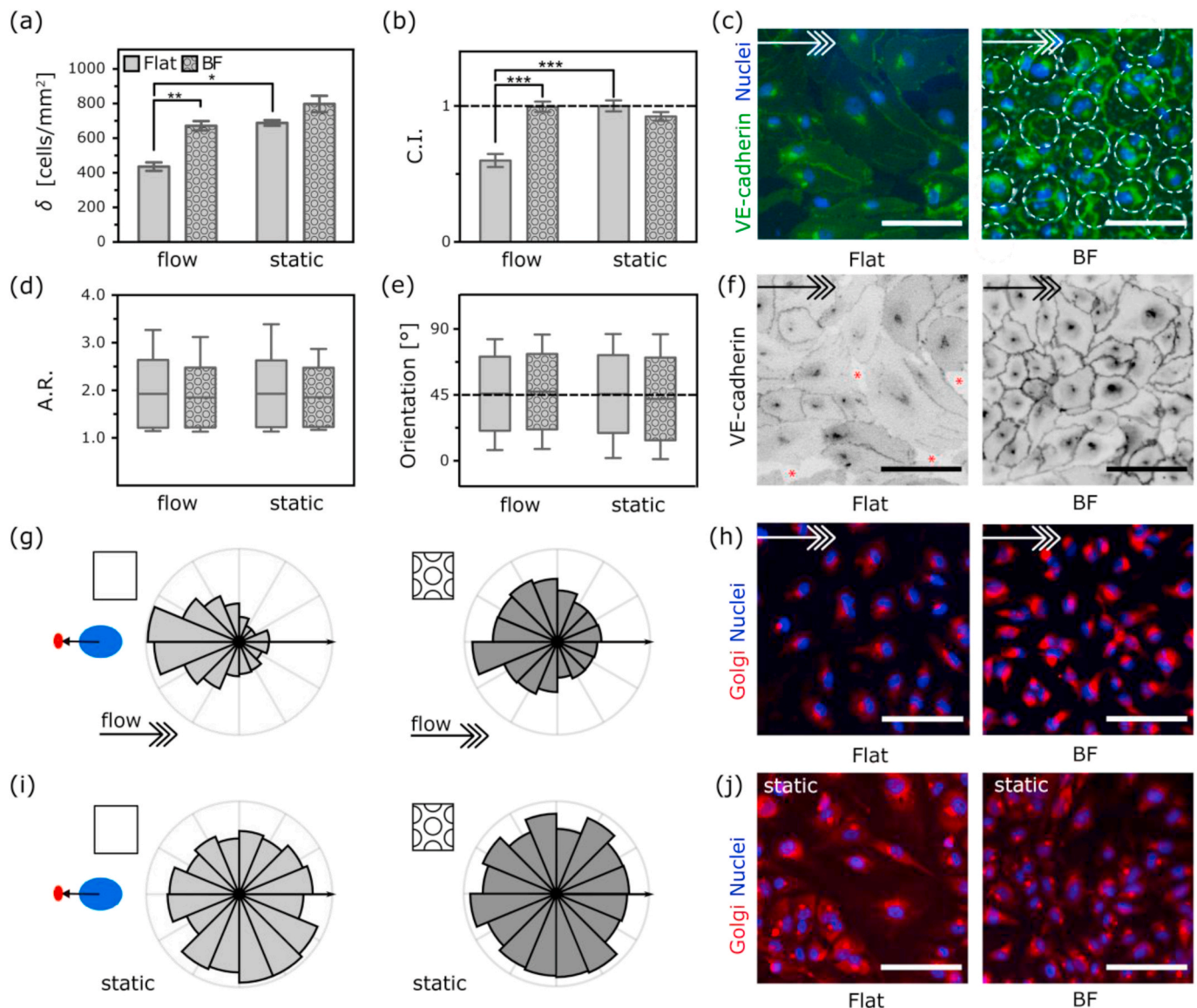


Fig. 5. Effect of flow magnitude on EC monolayers. Mature monolayers were exposed to an initial flow generating a WSS of 8 Pa for 12 h. The flow intensity was then sharply decreased to reach the WSS of 1.4 Pa for additional 6–8 h. Results of a representative experiment are shown. Experiment repetitions $N = 3$, data corresponding to the independent repetitions can be found in [Supplementary Material Figure S9](#). (a) Quantification of cell density (δ). Fields of view quantified in each bar $n = 10$. Data are expressed as mean \pm s.e.m. (b) Quantification of the connectivity index (C.I.). Results are normalized with respect to the average value of C.I. in static cultivation on flat surface. Number of cells quantified in each bar $n = 60$. C.I. of a fully connected EC monolayer (1) is indicated by a dashed line. (c) Immunostaining of EC monolayers seeded on flat (Flat, left) or BF substrates (BF, right). VE-cadherin (green) and cell nuclei (DAPI, blue). The corresponding bright field image (white) is overlaid on the BF image. The arrow indicates the flow direction. The BF wells are depicted by white dashed circles. Scale bar: 100 μ m. (d) Quantification of cell aspect ratio (A.R.). Boxes indicate mean \pm SD and whiskers indicate 5–95th percentile. Number of cells quantified in each box $n = 108$. (e) Quantification of cell orientation. Number of cells quantified in each box $n = 108$. Mean orientation of randomly oriented cells (45°) is indicated by a dashed line. (f) Immunostaining of endothelial cell monolayer on flat (Flat, left) or BF substrates (BF, right). VE-cadherin (grayscale inverted). The presence of gaps in the monolayer is highlighted by red asterisks. The arrow indicates the flow direction. Scale bar: 100 μ m. (g) Analysis of cell polarization in presence of WSS. Polar histograms reporting cell polarity assessment (vector pointing from nucleus to Golgi apparatus, as depicted in the drawing) on flat (left) or BF substrates (right). The arrow indicates the flow direction. Approximately $n = 1500$ cells were analyzed in each polar diagram. (h) Immunostaining of endothelial cell monolayer on flat (Flat, left) or BF substrates (BF, right), under flow. Golgi apparatus (red) and cell nuclei (DAPI, blue). Scale bar: 100 μ m. (i) Analysis of cell polarization in static conditions. Polar histograms reporting cell polarity assessment (vector pointing from nucleus to Golgi apparatus, as depicted in the drawing) on flat (Flat, left) and BF substrates (BF, right) in static conditions. (j) Immunostaining of EC monolayers seeded on flat (Flat, left) and BF substrates (BF, right) in static conditions. Golgi apparatus (red) and cell nuclei (DAPI, blue). Scale bar: 100 μ m. * $p < 0.05$, ** $p < 0.01$, *** $p < 0.001$. (For interpretation of the references to colour in this figure legend, the reader is referred to the Web version of this article.)

3.4. Endothelialization under disturbed flow: WSS magnitude

At vascular bifurcations, in presence of atherosclerotic plaques, or in correspondence of cardiovascular implants, ECs experience non-physiological hemodynamics characterized by high levels of WSS and steep variations in the flow magnitude. We therefore challenged the endothelialization performance of BF-patterned substrates under supraphysiological WSS conditions and upon sudden variation to lower values.

In the initial phase of this experiment, mature monolayers were exposed to laminar flow generating a WSS of 8 Pa (12 h). As expected, ECs on the flat region gradually oriented orthogonally to the flow

direction [28] and collectively polarized against the flow on the flat surface (Supplementary Material Video S3, Supplementary Material Figure S8). The degree of orientation and collective polarization was significantly reduced on BF-patterned substrates. After full adaptation was accomplished (Supplementary Material Video S3 and S4), the sample was subjected to a drop of flow magnitude (to WSS = 1.4 Pa).

The steep change in WSS rapidly compromised the integrity of the monolayer contacting the flat region with a significant reduction of density and connectivity ($\delta = 435 \pm 25$ cells/mm² and C.I. = 0.59 \pm 0.05; Fig. 5a and b, respectively). Gaps between cells and disassembly of cell-to-cell junctions were also apparent. The BF-patterned substrate locally protected the endothelium, which in this region maintained

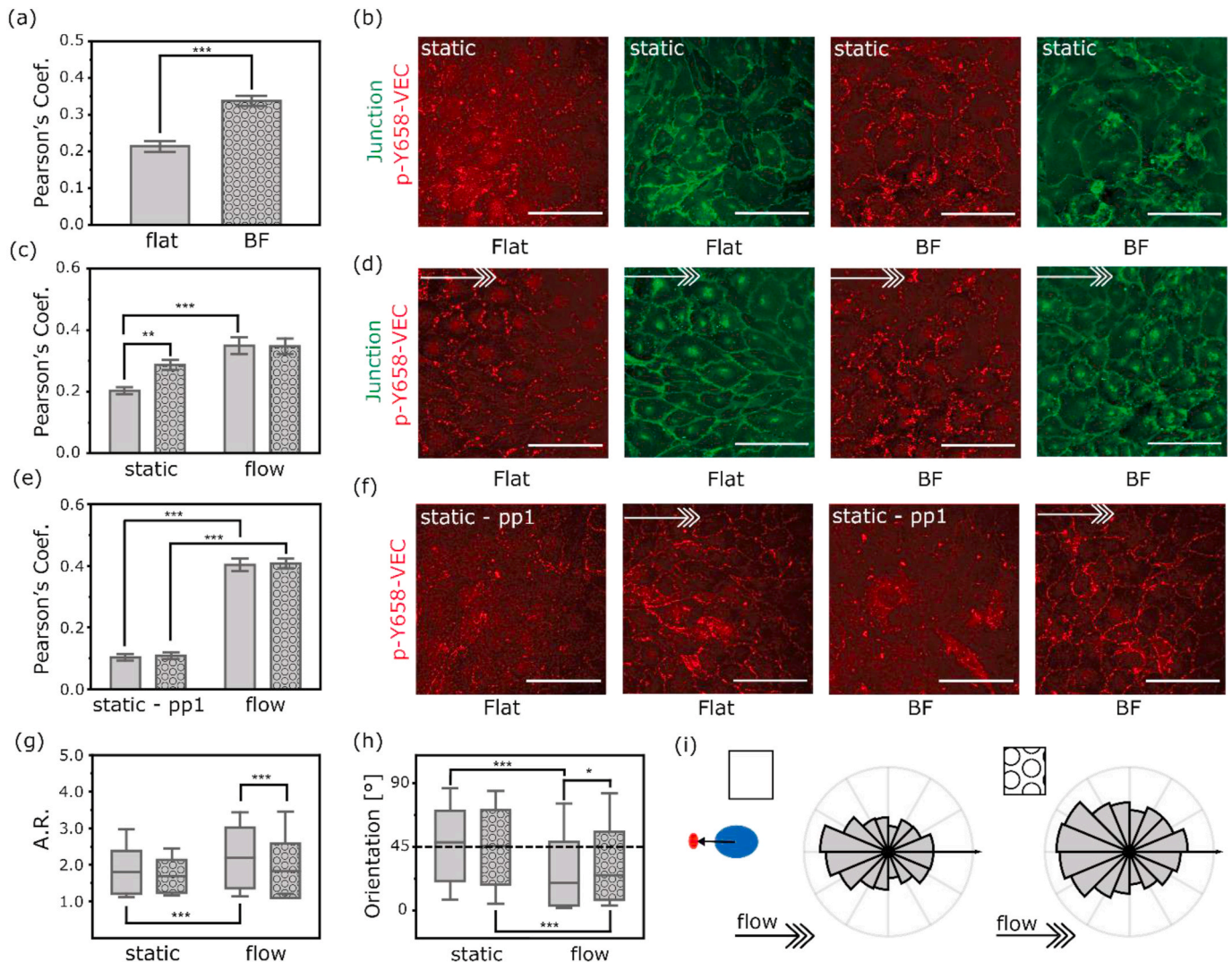


Fig. 6. Characterization of VE-Cadherin phosphorylation level at cellular junctions. N = 2. (a) The level of VE-Cadherin phosphorylation under static conditions. The phosphorylation level is measured as the Pearson's colocalization coefficient between the adherens junctions (AJs) marker β -catenin and p-Y658-VEC. Data are expressed as mean \pm s.e.m. (b) Immunostaining of EC monolayer on flat (Flat) or BF substrates (BF) under static condition. The β -catenin localization is depicted in green (junction) while the p-Y658-VEC signal is in red. Scale bar: 100 μ m. (c) VE-Cadherin phosphorylation in monolayers exposed to flow generating WSS of 1.4 Pa. Results on flat surface and BF surface under static culturing condition (static) and flow condition (flow) are presented. Data are expressed as mean \pm s.e.m. (d) The β -catenin localization is depicted in green (junction) while the p-Y658-VEC signal is in red. Scale bar: 100 μ m. (e) Corresponding levels of VE-Cadherin phosphorylation level upon inhibition treatment with the Src inhibitor pp-1. Results on flat surface and BF surface under static inhibition condition (static) and flow recovery condition (flow) are presented. Data are expressed as mean \pm s.e.m. (f) Immunostaining of EC monolayer on flat (Flat) or BF substrates (BF) under both static (static-pp1) and flow (flow arrow) condition. Scale bar: 100 μ m. (g) Quantification of cell aspect ratio (A.R.). Boxes indicate mean \pm SD and whiskers indicate 5-95th percentile. Number of cells quantified in each box n = 108. (h) Quantification of cell orientation. Number of cells quantified in each box n = 108. Mean orientation of randomly oriented cells (45°) is indicated by a dashed line. (i) Analysis of cell polarization in presence of 1.4 Pa WSS. Polar histograms reporting cell polarity assessment (vector pointing from nucleus to Golgi apparatus, as depicted in the drawing) on flat (left) or BF substrates (right). The arrow indicates the flow direction. Approximately n = 1500 cells were analyzed in each polar diagram. All arrows indicate flow direction. *p < 0.05, **p < 0.01, ***p < 0.001. (For interpretation of the references to colour in this figure legend, the reader is referred to the Web version of this article.)

uncompromised integrity and high cellular density ($\delta = 671 \pm 27$ cells/mm² C.I. = 1.0 ± 0.1 ; Fig. 5a and b, respectively). Individual cell shape (A.R. = 1.93 ± 0.71 and 1.84 ± 0.63 on flat or BF; respectively) and global orientation ($45^\circ \pm 25^\circ$ and $47^\circ \pm 26^\circ$ on flat or BF; respectively) were similar across the sample, indicating no specific adaptation to flow (Fig. 5d, e and 5f) after the reduction of the flow magnitude. A preferential counterflow polarization was instead observed on the flat surface (Fig. 5g and h, left). The same polarization was present ECs contacting the BF (Fig. 5g and h, right), but to a lesser extent. The polarization data of static control group is reported in Fig. 5i and j.

In summary, these data demonstrate that the interaction with BF-patterned surfaces preserves the monolayer connectivity and density upon steep variations of flow directionality or magnitude, yielding superior endothelialization performance as compared to identical, flat substrates.

3.5. Molecular changes in endothelial monolayers interacting with BF substrates

ECs undergo dramatic shape change and re-orientation in response to different levels of WSS [28,41,60]. Their adaptation to flow provides an exquisite example in which all cells in a monolayer undergo a common morphological response to a synchronized stimulus. This includes the dynamic turnover of AJs, the primary sites of mechanical coupling between ECs [60], which have important implications for endothelial homeostasis [41,61,62]. Upon flow stimulation, the coordinate remodeling of AJ complexes, which act as sensors and transducers of WSS [63–65], enables the cell shape change. A pivotal role in this process is played by VE-cadherin tyrosine phosphorylation [42]. In particular, the phosphorylation in Y658 is essential for flow sensing through the junctional complex and for the ensuing vascular remodeling both *in vitro* and *in vivo* [42].

Dynamic changes of VE-cadherin Y658 phosphorylation were therefore monitored upon flow exposure of endothelial monolayers grown on flat or BF-patterned substrates (Fig. 6). In agreement with previous reports [41,42], endothelia on flat substrates showed low levels of junctional VE-cadherin phosphorylation in static conditions (Fig. 6a and b). Phosphorylation was significantly increased upon exposure to physiological hemodynamic conditions (WSS of 1.4 Pa; Fig. 6c and d) followed by the collective orientation of ECs along the direction of flow and counterflow polarization (Supplementary Material Figure S5). On the other hand, on BF-patterned substrates, the levels of VE-cadherin phosphorylation were high in resting conditions (Fig. 6a) and were not significantly increased by the exposure to flow (WSS of 1.4 Pa, Fig. 6c and d). Steady levels of VE-cadherin phosphorylation correlated with limited cell orientation (Supplementary Material Figure S5d, S5e and S5f).

EC alignment in response to flow, requires a global increase of Y658 phosphorylation levels [42]. To evaluate whether the absence of VE-cadherin phosphorylation increase upon flow stimulation is hindering cell reorientation on BF-patterned substrates, the basal Y658 phosphorylation was artificially reduced using the Src inhibitor PP1 (Fig. 6e and f [41,42,66]). The ensuing exposure to flow triggered an increase of Y658 phosphorylation of VE-cadherin, on both flat and BF-patterned substrates. Importantly, in these conditions, alignment to flow was partially restored on BF patterns (Fig. 6g and h). In addition, ECs exhibited stronger polarization against the flow, as compared to the non-treated condition (Fig. 6i and Supplementary Material Figure S5g).

These data suggest that the effect of BF patterns is twofold. Firstly, flow diversion impinges in the directional signal provided by the local hemodynamic conditions and thus limits the collective reorganization of ECs, i.e. the alignment and polarization, on patterned substrates (Supplementary Material Figure S5d–j). In fact, signal mitigation is more prominent under supraphysiological WSS levels, due to the higher Reynolds number ([67,68], the effect can be seen in Supplementary Material Figure S8). Secondly, the BF topography interferes with the

molecular response triggered by the local hemodynamic conditions. Specifically, it hinders the post-translation modifications orchestrating the dynamic changes of AJs stability and enabling cell shape remodeling.

3.6. Generation and endothelialization of non-planar BF-patterned surfaces

Finally, we aimed at demonstrating that non-planar surfaces are conducive to the generation of BF-patterns supporting their endothelialization. To address this issue, a quarter section of a cylindrical pipe with internal diameter of 11 mm was selected as target geometry (Fig. 7a). The BF fabrication protocol developed for planar substrates (Fig. 1) was applied to the luminal pipe surface upon coating with RTV. Here, depending on the applied protocol, the BF formation resulted in larger W_{dia} (77 ± 13 μ m, Fig. 7b left) and W_{c2c} (114 ± 25 μ m Fig. 7b middle), and shallower W_{dep} (4.3 ± 0.6 μ m, Fig. 7b right) yielding suboptimal endothelialization performance (Supplementary Material Figure S7). Optimization of the curing protocol allowed to successfully generate protective BF structures (Fig. 7e, Table 1). Importantly, the distribution of topographical parameters consistently showed an overlapping range with the one obtained on planar surfaces. Additionally, the generation of BF patterns in the same range was demonstrated on the entire external surface of enameled copper wires (Fig. 7f).

ECs seeding led to the generation of confluent and mature endothelia in all similar to those obtained on planar BF substrates in static culture (Fig. 7c and d). The monolayer closely followed the curvature covering the entire internal surface of the tube (Fig. 7c and d). In summary, these results demonstrate the feasibility of the proposed fabrication approach on free-form, complex substrates comprising a silicon interface.

4. Discussion

The adaptation of connected cell monolayers to the local environmental conditions, created by the combination of biological and physical stimuli, requires the collective remodeling of individual cells [26]. Coordinated shape changes and orientation of the cell polarity define the ultimate structure of the endothelium, and altogether ensure its function [28]. The concept extends to the generation of hybrid interfaces, where ECs must interact with synthetic materials and conform to their architectures achieving a similar level of tissue functionality.

The human endothelium is a highly dynamic tissue in which cells maintain the ability to migrate and reshape in response to an apical flow. In static conditions, and in the absence of other directional signals, ECs assemble without preferential orientation or polarization. The immature, isotropic ensemble retains full adaptability [28,56,61]. The onset of flow, and the resulting WSS, primes the system inducing a gradual adaptation to the local hemodynamic conditions. In a developing organism, this process supports the formation of a vascular tree in which the monolayer configuration locally optimizes to the flow and the vascular wall architecture [58,69]. It is however evident that once primed, endothelial monolayers become less adaptive [41], and vulnerable to sudden variations of the environmental signals guiding cell orientation and polarization.

The achievement of a stable tissue configuration is a determining factor towards the success or the failure of endothelialization strategies. The target device function, its inner architecture, and the deployment procedure create unstable flow conditions, forming regions where the reconstituted endothelium must respond to changing guidance.

Endothelialization strategies based on submicron and micro-topographies, generally anisotropic in nature, exploit the interaction between surface geometries and integrin adhesions at the basal side of ECs [21]. The physical confinement enforced by the topographic features (e.g. the ridges of anisotropic gratings) guides not only the focal adhesion establishment and maturation but also the overall cell orientation, along the direction dictated by the gratings. This effect, termed

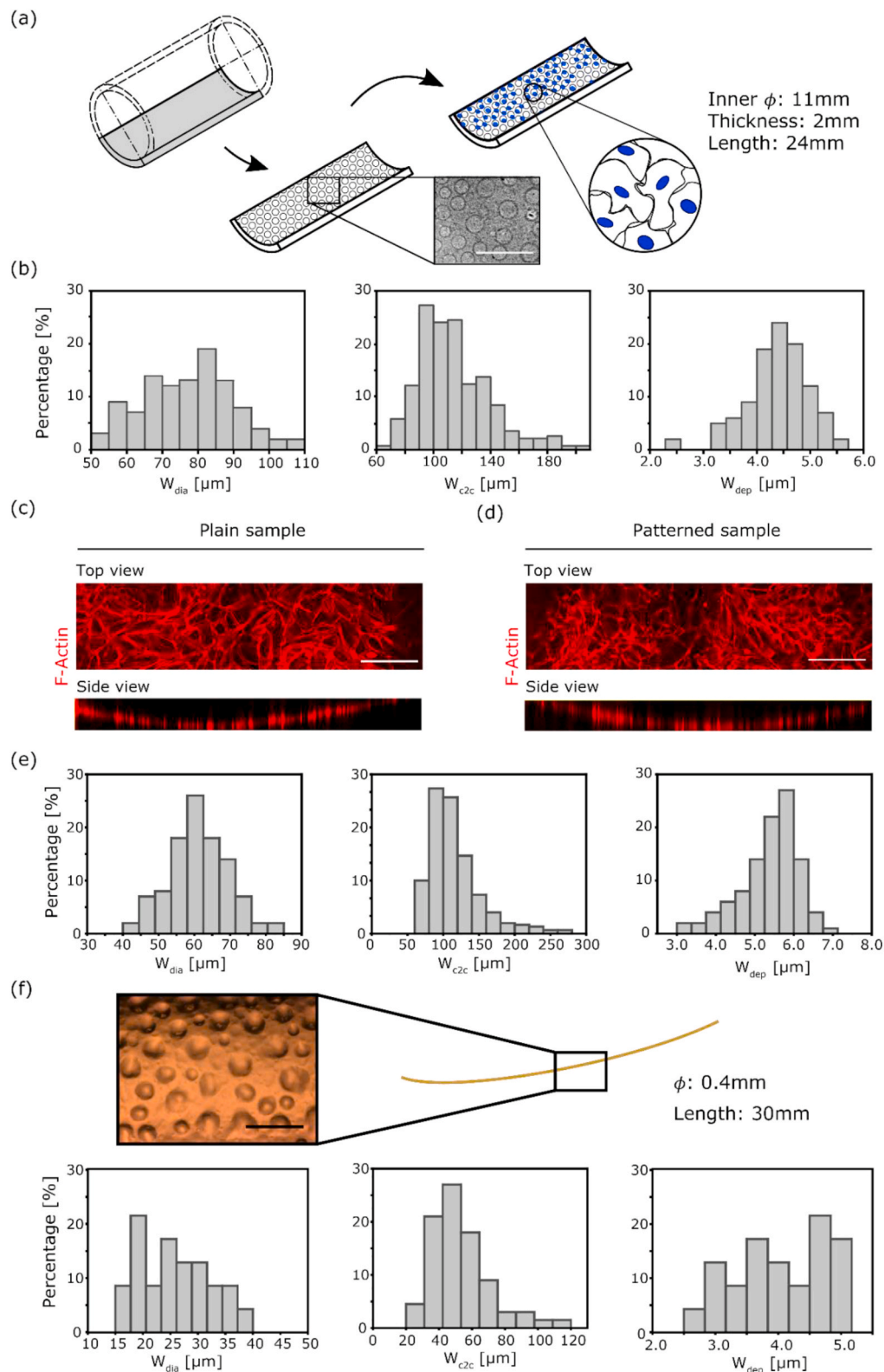


Fig. 7. Application of BF topography to non-planar surfaces. (a) Schematic representation of the non-planar surface. A section of a pipe was coated with RTV4420 and patterned with BF, scale bar: 200 μm . HUVECs were seeded on the gelatin-coated surface and cultured to examine the monolayer integrity. (b) Generation of shallow topography featuring well diameter (W_{dia} ; left), center-to-center distance (W_{c2c} ; middle) and depth (W_{dep} ; right). (c) Immunostaining of the reconstituted EC monolayer reporting the distribution of F-Actin (red) on top and side view. Scale bar: 200 μm . (d) Corresponding immunostaining of the BF patterned sample. Scale bar: 200 μm . (e) Generation of protective topography: well diameter (W_{dia} ; left), center-to-center distance (W_{c2c} ; middle) and depth (W_{dep} ; right). (f) Illustration depicting BF patterned thin wire (upper, scale bar: 50 μm) and the corresponding topography characterization: well diameter (W_{dia} ; lower left), center-to-center distance (W_{c2c} ; lower middle) and depth (W_{dep} ; lower right). (For interpretation of the references to colour in this figure legend, the reader is referred to the Web version of this article.)

contact guidance, supports endothelialization by inducing collective cell alignment along the flow or perpendicular to it [28]. This latter configuration extends the monolayer survival under supraphysiologic hemodynamic settings [28].

Unstable and detrimental variations of hemodynamic conditions are experienced at the luminal surface of cardiovascular implants. Here, the device function or the presence of deformable elements can locally induce sharp variations of flow intensity and directionality which pose a different challenge to the maintenance of a connected endothelium. Indeed, a change of WSS (from 8 to 1.4 Pa) or flow directionality, rapidly compromises endothelialization on flat substrates, leading to the loss of tissue integrity and substrate denudation (Figs. 4 and 5).

Flow-diverging structures provide an innovative solution to this problem. The rationale of this approach, originally developed for engineering applications, is to decompose the apical flow into a tessellation of local directions unable to provide global guidance. An isotropic tissue configuration, in which individual cells do not orient or polarize collectively along the same direction, is maintained in these conditions. The same structures buffer changes of flow directionality (Fig. 4) and intensity (Fig. 5). The BF topography not only physically interacts with the near-field flow, dampening its detrimental signals, but additionally interferes with the WSS-related cell response at the level of cell junctions in the monolayer (Fig. 6). In all tested conditions, ECs interacting with BF-patterned substrates limit their commitment to the imposed hemodynamic conditions (Figs. 2 and 3) and yield monolayer not primed by flow. These monolayers can resist to sharp changes of flow directionality or intensity (Figs. 4 and 5).

The complexity and diversity of implant materials at the luminal interface of blood contacting devices is what currently limits the application of surface topography as strategy to improve endothelialization and compatibility. Each different material (e.g. metals, plastic polymers, and others) requires dedicated protocols for the implementation of surface geometries, adding to the inherent technical challenges of applying surface modifications to non-planar architectures. Our envisioned strategy is to create a coating layer on which topography can be formed without the need of surface lithography. This intervening layer shall uniformly cover all luminal surfaces providing a conformal substrate conducive to the generation of BF. In this frame, the second key innovative element of this study is represented by the facile self-assembly process adopted to generate flow-diverging structures on the surface of elastomeric materials (Fig. 1). The resulting patterned surfaces are conducive to endothelialization, allowing for the generation of mature, isotropic monolayers identical to those obtained on corresponding flat substrates (Fig. 2). When exposed to flow or to sudden hemodynamic perturbations similar to those experienced at the luminal surface of cardiovascular devices, these endothelia do not show signs of adaptation and maintain their isotropic configuration. More importantly, they are able to survive perturbations which otherwise induce tissue denudation (Figs. 4 and 5). BF formation is an intrinsically free-form fabrication procedure, which perfectly applies to non-planar interfaces (Fig. 7). The dynamic regulation of temperature, relative humidity and material curing yields sufficient control over the size and distribution of resulting topographic features (Fig. 1) and thus opens to its implementation at the luminal surface of complex devices.

The endothelialization of cardiovascular implants can be achieved via alternative cell seeding processes [7]. In the *in vitro* endothelialization approach, the target substrates are seeded with ECs prior to deployment [47] to induce the formation of confluent monolayers in static conditions, which shall then be maintained upon device deployment and actuation. Alternatively, the luminal substrates can be endothelialized *in vivo*. In this approach, the bare device is initially implanted and its colonization by autologous endothelial cells is obtained from the luminal surface of neighboring vessels, via transmural ingrowth [70] or via adhesion and proliferation of circulating precursors [9].

In this frame, the ultimate demonstration of our proposed fabrication and endothelialization strategy shall be obtained in animal studies

showing the safety, compatibility, and efficacy of the technology (i.e. the long term integration in contact with blood, with avoidance of related complications such as thrombosis and blood damage) applied to the selected EC seeding procedure. For this, a chronic, large animal model will be required yielding statistical demonstration of the maintenance of a confluent and connected endothelial monolayer enabling the desired protective effect against adverse events [9].

In summary, the generation of BF establishes a valid method to realize the endothelialization of non-planar, complex surfaces under detrimental hemodynamic conditions of sharp flow intensity or directionality variations. This goes in the direction of implementing a viable and up-scalable technology to realistic, 3D architectures of cardiovascular devices, where the patterning with lithographic approaches is technically challenging. The method proposed here is fundamentally a controllable, self-assembly procedure yielding quasi-regular topographic features that support the generation of confluent and connected endothelia. In all these aspects, the technology at hand is superior to other topographic approaches so far developed.

5. Conclusions

Endothelialization of complex cardiovascular devices requires innovative approaches to ensure the maintenance of a protective autologous endothelium under challenging hemodynamic conditions created by the implant deployment and function. Flow-diversion and mitigation of endothelial cells response to WSS, hampers the noxious environmental stimuli generated by sudden variation of flow directionality or magnitude, thus preserving the tissue integrity. Topographic features interacting with flow are introduced on the surface of silicone materials by means of a self-assembly process harnessing water droplet condensation upon material curing and yielding the controlled imprint of moon-crater shapes with cell length-scale dimensions. The procedure is intrinsically free-form and immediately conducive to the patterning of complex, three-dimensional architectures at the luminal implant surface.

Declaration of competing interest

The authors declare the following financial interests/personal relationships which may be considered as potential competing interests: XW, AK, RH, EM and AF have filed a patent (EP20208958.7) for protection of the technology described in the manuscript. All other authors have no interest to declare.

Acknowledgements

This work is part of the Zurich Heart project under the umbrella of "Hochschulmedizin Zürich" and is supported by the Stavros Niarchos Foundation.

This work is also supported by funding from the Swiss National Science Foundation (SNF), Grant 205321_188828.

Appendix A. Supplementary data

Supplementary data to this article can be found online at <https://doi.org/10.1016/j.biomaterials.2021.120816>.

Data availability

The raw/processed data required to reproduce these findings cannot be shared at this time due to technical or time limitations.

Author statement

Xi Wu: conceptualization, investigation, methodology, validation, formal analysis, writing - original draft, review and editing,

visualization. Silvia Moimas: investigation, validation, resources, writing – original draft, writing - review and editing, visualization. Raoul Hopf: conceptualization, methodology, investigation, supervision. Costanza Giampietro: investigation, methodology, conceptualization, writing – review and editing. Andreas Kourouklis: investigation, writing – review and editing. Volkmar Falk: project administration, supervision. Edoardo Mazza: conceptualization, supervision, writing – review and editing, funding acquisition. Aldo Ferrari: conceptualization, supervision, writing – review and editing, funding acquisition, project administration.

References

- [1] Y. Chandorkar, K. Ravikumar, B. Basu, The foreign body response demystified, *ACS Biomater. Sci. Eng.* 5 (2019) 19–44, <https://doi.org/10.1021/acsbomaterials.8b00252>.
- [2] D.W. Grainger, All charged up about implanted biomaterials, *Nat. Biotechnol.* 31 (2013) 507–509, <https://doi.org/10.1038/nbt.2600>.
- [3] J.M. Anderson, A. Rodriguez, D.T. Chang, Foreign body reaction to biomaterials, *Semin. Immunol.* 20 (2008) 86–100, <https://doi.org/10.1016/j.smim.2007.11.004>.
- [4] I.H. Jaffer, J.C. Fredenburgh, J. Hirsh, J.I. Weitz, Medical device-induced thrombosis: what causes it and how can we prevent it? *J. Thromb. Haemostasis* 13 (2015) S72–S81, <https://doi.org/10.1111/jth.12961>.
- [5] S. Susen, A. Rauch, E. Van Belle, A. Vincentelli, P.J. Lenting, Circulatory support devices: fundamental aspects and clinical management of bleeding and thrombosis, *J. Thromb. Haemostasis* 13 (2015) 1757–1767, <https://doi.org/10.1111/jth.13120>.
- [6] M. Schmid Daners, F. Kaufmann, R. Amacher, G. Ochsner, M.J. Wilhelm, A. Ferrari, E. Mazza, D. Poulikakos, M. Meboldt, V. Falk, Left ventricular assist devices: challenges toward sustaining long-term patient care, *Ann. Biomed. Eng.* 45 (2017) 1836–1851, <https://doi.org/10.1007/s10439-017-1858-9>.
- [7] S. Jana, Endothelialization of cardiovascular devices, *Acta Biomater.* 99 (2019) 53–71, <https://doi.org/10.1016/j.actbio.2019.08.042>.
- [8] A.J. Melchiorri, N. Hibino, J.P. Fisher, Strategies and techniques to enhance the in situ endothelialization of small-diameter biodegradable polymeric vascular grafts, *Tissue Eng. B Rev.* 19 (2013) 292–307, <https://doi.org/10.1089/ten.teb.2012.0577>.
- [9] G.M. Rubanyi, The role of endothelium in cardiovascular homeostasis and diseases, in: *J. Cardiovasc Pharmacol* (Ed.), J. Cardiovasc Pharmacol, 1993, <https://doi.org/10.1097/00005344-199322004-00002>.
- [10] S.J. Sonntag, T.A.S. Kaufmann, M.R. Büsen, M. Laumen, T. Linde, T. Schmitz-Rode, U. Steinseifer, Simulation of a pulsatile total artificial heart: development of a partitioned Fluid Structure Interaction model, *J. Fluid Struct.* 38 (2013) 187–204, <https://doi.org/10.1016/j.jfluidstructs.2012.11.011>.
- [11] L. Wiegmann, B. Thamsen, D. de Zélicourt, M. Granegger, S. Boës, M. Schmid Daners, M. Meboldt, V. Kurtcuoglu, Fluid dynamics in the HeartMate 3: influence of the artificial pulse feature and residual cardiac pulsation, *Artif. Organs* 2019 (2018) 363–376, <https://doi.org/10.1111/aor.13346>.
- [12] B.J. Bachmann, L. Bernardi, C. Loosli, J. Marschewski, M. Perrini, M. Ehrbar, P. Ermanni, D. Poulikakos, A. Ferrari, E. Mazza, A novel bioreactor system for the assessment of endothelialization on deformable surfaces, *Sci. Rep.* 6 (2016), <https://doi.org/10.1038/srep38861>.
- [13] C. Wang, B.M. Baker, C.S. Chen, M.A. Schwartz, Endothelial cell sensing of flow direction, *Arterioscler. Thromb. Vasc. Biol.* 33 (2013) 2130–2136, <https://doi.org/10.1161/ATVBAHA.113.301826>.
- [14] H.B. Kwon, S. Wang, C. Helker, et al., In vivo modulation of endothelial polarization by Apelin receptor signalling, *Nat. Commun.* 7 (2016) 11805, <https://doi.org/10.1038/ncomms11805>.
- [15] P.F. Davies, Flow-mediated endothelial mechanotransduction, *Physiol. Rev.* 75 (1995) 519–560, <https://doi.org/10.1152/physrev.1995.75.3.519>.
- [16] S. Mccue, D. Dajnowicz, F. Xu, M. Zhang, M.R. Jackson, B.L. Langille, Shear Stress Regulates Forward and Reverse Planar Cell Polarity of Vascular Endothelium in Vivo and in Vitro, 2006, <https://doi.org/10.1161/01.RES.0000216595.15868.55>.
- [17] P.M. Ligrani, J.L. Harrison, G.I. Mahmod, M.L. Hill, Flow structure due to dimple depressions on a channel surface, *Phys. Fluids* 13 (2001) 3442–3451, <https://doi.org/10.1063/1.1404139>.
- [18] A. Dewan, P. Srivastava, A review of heat transfer enhancement through flow disruption in a microchannel, *J. Therm. Sci.* 24 (2015) 203–214, <https://doi.org/10.1007/s11630-015-0775-1>.
- [19] N.K. Burgess, M.M. Oliveira, P.M. Ligrani, Nusselt number behavior on deep dimpled surfaces within a channel, in: *ASME Int. Mech. Eng. Congr. Expo. Proc.*, American Society of Mechanical Engineers (ASME), 2002, pp. 49–57, <https://doi.org/10.1115/IMECE2002-32941>.
- [20] B. Geiger, J.P. Spatz, A.D. Bershadsky, Environmental sensing through focal adhesions, *Nat. Rev. Mol. Cell Biol.* 10 (2009) 21–33, <https://doi.org/10.1038/nrm2593>.
- [21] E. Potthoff, D. Franco, V. D'Alessandro, C. Starck, V. Falk, T. Zambelli, J. A. Vorholt, D. Poulikakos, A. Ferrari, Toward a rational design of surface textures promoting endothelialization, *Nano Lett.* 14 (2014) 1069–1079, <https://doi.org/10.1021/nl4047398>.
- [22] D. Franco, M. Klingauf, M. Bednarzik, M. Cecchini, V. Kurtcuoglu, J. Gobrecht, D. Poulikakos, A. Ferrari, Control of initial endothelial spreading by topographic activation of focal adhesion kinase, *Soft Matter* 7 (2011) 7313–7324, <https://doi.org/10.1039/c1sm05191a>.
- [23] D. Franco, F. Milde, M. Klingauf, F. Orsenigo, E. Dejana, D. Poulikakos, M. Cecchini, P. Koumoutsakos, A. Ferrari, V. Kurtcuoglu, Accelerated endothelial wound healing on microstructured substrates under flow, *Biomaterials* 34 (2013) 1488–1497, <https://doi.org/10.1016/j.biomaterials.2012.10.007>.
- [24] B.J. Bachmann, C. Giampietro, A. Bayram, G. Stefopoulos, C. Michos, G. Graeber, M.V. Falk, D. Poulikakos, A. Ferrari, Honeycomb-structured metasurfaces for the adaptive nesting of endothelial cells under hemodynamic loads, *Biomater. Sci.* 6 (2018) 2726–2737, <https://doi.org/10.1039/c8bm00660a>.
- [25] G. Stefopoulos, C. Giampietro, V. Falk, D. Poulikakos, A. Ferrari, Facile endothelium protection from TNF- α inflammatory insult with surface topography, *Biomaterials* 138 (2017) 131–141, <https://doi.org/10.1016/j.biomaterials.2017.05.039>.
- [26] G. Stefopoulos, F. Robotti, V. Falk, D. Poulikakos, A. Ferrari, Endothelialization of rationally microtextured surfaces with minimal cell seeding under flow, *Small* 12 (2016) 4113–4126, <https://doi.org/10.1002/sml.201503959>.
- [27] S. Antonini, S. Meucci, E. Jacchetti, M. Klingauf, F. Beltram, D. Poulikakos, M. Cecchini, A. Ferrari, Sub-micron lateral topography affects endothelial migration by modulation of focal adhesion dynamics, *Biomed. Mater.* 10 (2015), 035010, <https://doi.org/10.1088/1748-6041/10/3/035010>.
- [28] F. Robotti, D. Franco, L. Bänninger, J. Wyler, C.T. Starck, V. Falk, D. Poulikakos, A. Ferrari, The influence of surface micro-structure on endothelialization under supraphysiological wall shear stress, *Biomaterials* 35 (2014) 8479–8486, <https://doi.org/10.1016/j.biomaterials.2014.06.046>.
- [29] S. Lakshminarayanan, Micro/nano patterning on polymers using soft lithography technique, in: *Micro/Nanolithography - A Heuristic Asp. Endur. Technol.*, InTech, 2018, <https://doi.org/10.5772/intechopen.72885>.
- [30] A. Colas, J. Curtis, Silicones, in: *Handb. Polym. Appl. Med. Med. Devices*, Elsevier Inc., 2013, pp. 131–143, <https://doi.org/10.1016/B978-0-323-22805-3.00007-4>.
- [31] A. Carré, M.E.R. Shanahan, Effect of cross-linking on the dewetting of an elastomeric surface, *J. Colloid Interface Sci.* 191 (1997) 141–145, <https://doi.org/10.1006/jcis.1997.4952>.
- [32] Z. Cao, A.V. Dobrynin, Polymeric droplets on soft surfaces: from Neumann's triangle to Young's law, *Macromolecules* 48 (2015) 443–451, <https://doi.org/10.1021/ma501672p>.
- [33] M.T. Calejo, T. Ilmarinen, H. Skottman, M. Kellomäki, Breath figures in tissue engineering and drug delivery: state-of-the-art and future perspectives, *Acta Biomater.* 66 (2018) 44–66, <https://doi.org/10.1016/j.actbio.2017.11.043>.
- [34] A. Rahimi, A. Mashak, Review on rubbers in medicine: natural, silicone and polyurethane rubbers, *Plast. Rubber Compos.* 42 (2013) 223–230, <https://doi.org/10.1179/1743289811Y.0000000063>.
- [35] H. Yabu, Fabrication of honeycomb films by the breath figure technique and their applications, *Sci. Technol. Adv. Mater.* 19 (2018) 802–822, <https://doi.org/10.1080/14686996.2018.1528478>.
- [36] L. Bernardi, R. Hopf, D. Sibilio, A. Ferrari, A.E. Ehret, E. Mazza, On the cyclic deformation behavior, fracture properties and cytotoxicity of silicone-based elastomers for biomedical applications, *Polym. Test.* 60 (2017) 117–123, <https://doi.org/10.1016/j.polymertesting.2017.03.018>.
- [37] *Bluestar-Silicones, Silbione® Rtv 4420 A/B Technical Datasheet*, 2019, pp. 11–13.
- [38] A. Baudot, J. Mazuer, J. Odin, Thermal conductivity of a RTV silicone elastomer between 1.2 and 300 K, *Cryogenics (Guildf)* 38 (1998) 227–230, [https://doi.org/10.1016/S0011-2275\(97\)00146-X](https://doi.org/10.1016/S0011-2275(97)00146-X).
- [39] S. Kashi, R. Varley, M. De Souza, S. Al-Asfari, A. Di Pietro, C. de Lavigne, B. Fox, Mechanical, thermal, and morphological behavior of silicone rubber during accelerated aging, *Polym. Plast. Technol. Eng.* 57 (2018) 1687–1696, <https://doi.org/10.1080/03602559.2017.1419487>.
- [40] K. Von Petersdorff-Campen, J. Abeken, D. De Zélicourt, V. Kurtcuoglu, M. Meboldt, M. Schmid Daners, In Vitro Testing and Comparison of Additively Manufactured Polymer Impellers for the CentriMag Blood Pump, *ASAIO J. Publish Ah*, 2020, <https://doi.org/10.1097/mat.0000000000001220>.
- [41] F. Orsenigo, C. Giampietro, A. Ferrari, M. Corada, A. Galaup, S. Sigismund, G. Ristagno, L. Maddaluno, G.Y. Koh, D. Franco, V. Kurtcuoglu, D. Poulikakos, P. Baluk, D. McDonald, M. Grazia Lampugnani, E. Dejana, Phosphorylation of VE-cadherin is modulated by haemodynamic forces and contributes to the regulation of vascular permeability in vivo, *Nat. Commun.* 3 (2012) 1208, <https://doi.org/10.1038/ncomms2199>.
- [42] D.E. Conway, B.G. Coon, M. Budatha, P.T. Arsenovic, F. Orsenigo, F. Wessel, J. Zhang, Z. Zhuang, E. Dejana, D. Vestweber, M.A. Schwartz, VE-cadherin phosphorylation regulates endothelial fluid shear stress responses through the polarity protein LGN, *Curr. Biol.* 27 (2017) 2219–2225, <https://doi.org/10.1016/j.cub.2017.06.020>, e5.
- [43] M.G. Lampugnani, M. Corada, L. Caveda, F. Breviaro, O. Ayalon, B. Geiger, E. Dejana, The molecular organization of endothelial cell to cell junctions: differential association of plakoglobin, β -catenin, and α -catenin with vascular endothelial cadherin (VE-cadherin), *J. Cell Biol.* 129 (1995) 203–217, <https://doi.org/10.1083/jcb.129.1.203>.
- [44] B. Forster, D. Van De Ville, J. Berent, D. Sage, M. Unser, Complex wavelets for extended depth-of-field: a new method for the fusion of multichannel microscopy images, *Microsc. Res. Tech.* 65 (2004) 33–42, <https://doi.org/10.1002/jemt.20092>.
- [45] F.M. Pramotton, F. Robotti, C. Giampietro, T. Lendenmann, D. Poulikakos, A. Ferrari, Optimized topological and topographical expansion of epithelia, *ACS*

- Biomater. Sci. Eng. 5 (2019) 3922–3934, <https://doi.org/10.1021/acsbomaterials.8b01346>.
- [46] L. Bernardi, C. Giampietro, V. Marina, M. Genta, E. Mazza, A. Ferrari, Adaptive reorientation of endothelial collectives in response to strain, *Integr. Biol. (United Kingdom)* 10 (2018) 527–538, <https://doi.org/10.1039/c8ib00092a>.
- [47] A. Ferrari, C. Giampietro, B. Bachmann, L. Bernardi, D. Bezuidenhout, P. Ermanni, R. Hopf, S. Kitz, G. Kress, C. Loosli, V. Marina, M. Meboldt, G. Pellegrini, D. Poulikakos, M. Rebholz, M. Schmid Daners, T. Schmidt, C. Starck, G. Stefopoulos, S. Sündermann, B. Thamsen, P. Zilla, E. Potapov, V. Falk, E. Mazza, A novel hybrid membrane VAD as first step toward hemocompatible blood propulsion, *Ann. Biomed. Eng.* 49 (2021) 716–731, <https://doi.org/10.1007/s10439-020-02590-1>.
- [48] D. Guan, Z. Cai, X. Liu, B. Lou, Y. Dou, D. Xu, W. Yao, Rheological study on the cure kinetics of two-component addition cured silicone rubber *, *Chin. J. Polym. Sci.* 34 (2016), <https://doi.org/10.1007/s10118-016-1847-8>.
- [49] J.Y. Chen, M. Hu, H. Zhang, B.C. Li, H. Chang, K.F. Ren, Y.B. Wang, J. Ji, Improved antithrombotic function of oriented endothelial cell monolayer on microgrooves, *ACS Biomater. Sci. Eng.* 4 (2018) 1976–1985, <https://doi.org/10.1021/acsbomaterials.7b00496>.
- [50] F. Neto, A. Klaus-Bergmann, Y.T. Ong, S. Alt, A.C. Vion, A. Szymborska, J. R. Carvalho, I. Hollfinger, E. Bartels-Klein, C.A. Franco, M. Potente, H. Gerhardt, YAP and TAZ regulate adherens junction dynamics and endothelial cell distribution during vascular development, *Elife* 7 (2018) 1–30, <https://doi.org/10.7554/eLife.31037>.
- [51] S. Dupont, L. Morsut, M. Aragona, E. Enzo, S. Giullitti, M. Cordenonsi, F. Zanconato, J. Le Diggabel, M. Forcato, S. Bicciato, N. Elvassore, S. Piccolo, Role of YAP/TAZ in mechanotransduction, *Nature* 474 (2011) 179–184, <https://doi.org/10.1038/nature10137>.
- [52] E. Tkachenko, E. Gutierrez, S.K. Saikin, P. Fogelstrand, C. Kim, A. Groisman, M. H. Ginsberg, The nucleus of endothelial cell as a sensor of blood flow direction, *Biol. Open* 2 (2013) 1007–1012, <https://doi.org/10.1242/bio.20134622>.
- [53] C. Wang, H. Lu, M. Alexander Schwartz, A novel in vitro flow system for changing flow direction on endothelial cells, *J. Biomech.* 45 (2012) 1212–1218, <https://doi.org/10.1016/j.jbiomech.2012.01.045>.
- [54] R.J. Steward, D. Tambe, C.C. Hardin, R. Krishnan, J.J. Fredberg, Fluid shear, intercellular stress, and endothelial cell alignment, *Am. J. Physiol. Cell Physiol.* 308 (2015) C657–C664, <https://doi.org/10.1152/ajpcell.00363.2014>.
- [55] M.A. Ostrowski, N.F. Huang, T.W. Walker, T. Verwijlen, C. Poplawski, A.S. Khoo, J. P. Cooke, G.G. Fuller, A.R. Dunn, Microvascular endothelial cells migrate upstream and align against the shear stress field created by impinging flow, *Biophys. J.* 106 (2014) 366–374, <https://doi.org/10.1016/j.bpj.2013.11.4502>.
- [56] E. Michalaki, V.N. Surya, G.G. Fuller, A.R. Dunn, Perpendicular alignment of lymphatic endothelial cells in response to spatial gradients in wall shear stress, *Commun. Biol.* 3 (2020) 1–9, <https://doi.org/10.1038/s42003-019-0732-8>.
- [57] H. Masuda, K. Kawamura, H. Nanjo, E. Sho, M. Komatsu, T. Sugiyama, A. Sugita, Y. Asari, M. Kobayashi, T. Ebina, N. Hoshi, T.M. Singh, C. Xu, C.K. Zarins, Ultrastructure of endothelial cells under flow alteration, *Microsc. Res. Tech.* 60 (2003) 2–12, <https://doi.org/10.1002/jemt.10237>.
- [58] J.J. Chiu, S. Chien, Effects of disturbed flow on vascular endothelium: pathophysiological basis and clinical perspectives, *Physiol. Rev.* 91 (2011) 327–387, <https://doi.org/10.1152/physrev.00047.2009>.
- [59] F. Gijssen, Y. Katagiri, P. Barlis, C. Bourantas, C. Collet, U. Coskun, J. Daemen, J. Dijkstra, E. Edelman, P. Evans, K. Van Der Heiden, R. Hose, B.K. Koo, R. Krams, A. Marsden, F. Migliavacca, Y. Onuma, A. Ooi, E. Poon, H. Samady, P. Stone, K. Takahashi, D. Tang, V. Thondapu, E. Tenekecioglu, L. Timmins, R. Torii, J. Wentzel, P. Serruys, Expert recommendations on the assessment of wall shear stress in human coronary arteries: existing methodologies, technical considerations, and clinical applications, *Eur. Heart J.* 40 (2019) 3421–3433, <https://doi.org/10.1093/eurheartj/ehz551>.
- [60] S. Noria, D.B. Cowan, A.I. Gotlieb, B.L. Langille, Transient and steady-state effects of shear stress on endothelial cell adherens junctions, *Circ. Res.* 85 (1999) 504–514, <https://doi.org/10.1161/01.RES.85.6.504>.
- [61] S. Chien, Mechanotransduction and endothelial cell homeostasis: the wisdom of the cell, in: *Am. J. Physiol. - Hear. Circ. Physiol.*, American Physiological Society, 2007, <https://doi.org/10.1152/ajpheart.01047.2006>.
- [62] C. Givens, E. Tzima, Endothelial mechanosignaling: does one sensor fit all? Antioxidants Redox Signal. 25 (2016) 373–388, <https://doi.org/10.1089/ars.2015.6493>.
- [63] E. Tzima, M. Irani-Tehrani, W.B. Kiosses, E. Dejana, D.A. Schultz, B. Engelhardt, G. Cao, H. DeLisser, M.A. Schwartz, A mechanosensory complex that mediates the endothelial cell response to fluid shear stress, *Nature* 437 (2005) 426–431, <https://doi.org/10.1038/nature03952>.
- [64] A. Angulo-Urarte, T. van der Wal, S. Huveneers, Cell-cell junctions as sensors and transducers of mechanical forces, *Biochim. Biophys. Acta Biomembr.* 1862 (2020), <https://doi.org/10.1016/j.bbamem.2020.183316>.
- [65] B.G. Coon, N. Baeyens, J. Han, M. Budatha, T.D. Ross, J.S. Fang, S. Yun, J. L. Thomas, M.A. Schwartz, Intramembrane binding of VE-cadherin to VEGFR2 and VEGFR3 assembles the endothelial mechanosensory complex, *J. Cell Biol.* 208 (2015) 975–986, <https://doi.org/10.1083/jcb.201408103>.
- [66] V. Aragon-Sanabria, S.E. Pohler, V.J. Eswar, M. Bierowski, E.W. Gomez, C. Dong, VE-cadherin disassembly and cell contractility in the endothelium are necessary for barrier disruption induced by tumor cells, *Sci. Rep.* 7 (2017) 1–15, <https://doi.org/10.1038/srep45835>.
- [67] S.D. Hwang, H.G. Kwon, H.H. Cho, Heat transfer with dimple/protrusion arrays in a rectangular duct with a low Reynolds number range, *Int. J. Heat Fluid Flow* 29 (2008) 916–926, <https://doi.org/10.1016/j.ijheatfluidflow.2008.01.004>.
- [68] A. Khalatov, D. Ochoa, A. Byerley, S.K. Min, Flow characteristics within and downstream of spherical and cylindrical dimple on a flat plate at low Reynolds numbers, in: *Proc. ASME Turbo Expo 2004, American Society of Mechanical Engineers Digital Collection*, 2004, pp. 589–601, <https://doi.org/10.1115/gt2004-53656>.
- [69] M. Simionescu, Endothelial cell response to normal and abnormal stimuli, in: *Endothel. Cell Dysfunctions*, Springer US, 1992, pp. 3–9, https://doi.org/10.1007/978-1-4899-0721-9_1.
- [70] T. Pennel, D. Bezuidenhout, J. Koehne, N.H. Davies, P. Zilla, Transmural capillary ingrowth is essential for confluent vascular graft healing, *Acta Biomater.* 65 (2018) 237–247, <https://doi.org/10.1016/j.actbio.2017.10.038>.